symmetry

MDPI

Article

Concomitant Observer-Based Multi-Level Fault-Tolerant Control for Near-Space Vehicles with New Type Dissimilar Redundant Actuation System

Meiling Wang [1], Jun Wang [2,*] and Jian Huang [2]

[1] Hope College, Southwest Jiaotong University, Chengdu 610400, China; sywang@my.swjtu.edu.cn
[2] Beijing Institute of Automatic Control Equipment, Beijing 100074, China; huangjian421@126.com
* Correspondence: dwill-wang@buaa.edu.cn

Abstract: This paper presents a concomitant observer-based multi-level fault-tolerant control (FTC) for near-space vehicles (NSVs) with a new type dissimilar redundant actuation system (NT-DRAS). When NSV flight control system faults occur in NT-DRAS and attitude-corresponding sensors, the NSV hybrid output states, including the concomitant observer usable states and the real system states, are applied to solve the FTC gain by using the linear quadratic regulator (LQR) technique. Furthermore, since NT-DRAS is used in NSVs, a multi-level (actuation system level and flight control level) FTC strategy integrating NT-DRAS channel switching and flight control LQR is proposed for complex and worsening fault cases. The most important finding is that though the proposed strategy is applicable for worsening fault cases in NSVs, systematic and accurate criteria for the process being performed are necessary and can improve the FTC efficiency with minimal FTC resources. Additionally, such criteria can improve the NSV's responsiveness to comprehensive faults, provided that the real-time performance of the fault detection and diagnosis (FDD) scheme can be further optimized. The concomitant observer convergence and the multi-level FTC strategy have been verified by numerical simulations based on the Matlab/Simulink platform.

Keywords: near-space vehicle; flight control system; new type dissimilar redundant actuation system; concomitant observer; multi-level fault-tolerant control

check for updates

Citation: Wang, M.; Wang, J.; Huang, J. Concomitant Observer-Based Multi-Level Fault-Tolerant Control for Near-Space Vehicles with New Type Dissimilar Redundant Actuation System. *Symmetry* **2024**, *16*, 1221. https://doi.org/10.3390/sym16091221

Academic Editor: Sergei D. Odintsov

Received: 17 August 2024
Revised: 6 September 2024
Accepted: 9 September 2024
Published: 17 September 2024

Copyright: © 2024 by the authors. Licensee MDPI, Basel, Switzerland. This article is an open access article distributed under the terms and conditions of the Creative Commons Attribution (CC BY) license (https://creativecommons.org/licenses/by/4.0/).

1. Introduction

High-value near-space vehicles (NSVs), with specific applications such as near-space exploration, have great significance and are attracting growing interest in not only academia but also industry [1,2]. NSVs should be designed with a high power/weight ratio, a high level of intelligence, and excellent reliability, and their hardware systems should support intelligent control algorithms. As an essential NSV subsystem, the actuation system is applied to realize flight and attitude control; therefore, it is defined as a safety system [3,4]. To ensure flight safety and further improve reliability, a hydraulic actuator (HA) and an electro-hydrostatic actuator (EHA) are designed and integrated as a dissimilar redundant actuation system (DRAS); such systems are widely used in large civil aircraft to avoid common-mode failures [5–7]. However, for NSVs with specific applications, an EHA and an electro-mechanical actuator (EMA) can be designed and integrated as a new type dissimilar redundant actuation system (NT-DRAS) with a higher power/weight ratio compared with former systems. An NT-DRAS can also provide fault-tolerant control (FTC) based on its dissimilar redundancy hardware [8], leading to higher mission reliability. Therefore, NT-DRASs are optimized actuation system schemes for NSVs. Attitude-corresponding sensor failure can lead the NSV states to be undetectable, and the state feedback control law cannot be performed using invalid states. Therefore, both NT-DRAS and sensor failures are essential factors for NSV flight safety.

As an important piece of flight safety technology, the FTC technique can be used to deal with actuator failure problems [9,10]. In some research works, this problem is modeled as a reliable robust flight tracking control one, where only a linear matrix inequality (LMI)-based control gain needs to be solved [11,12]. This kind of FTC controller is passive, since there is no controller reconfiguration. The adaptive technique is usually used in this case to enhance the passive FTC controller's level of control [13]. Once the passive controller cannot cope with the fault conditions, for example, when multiple faults occur, a hybrid FTC mechanism including normal, passive, and reconfigurable controllers is more effective and can achieve the desired FTC performance, even under changing actuator fault conditions [14]. However, these results do not consider sensor faults in a flight control system. A simultaneous fault condition with both actuator and sensor failures is more complex and severe, because the controllable actuation system channel is limited and some flight output states are unknown. This challenging issue has been studied in some research [15–17].

To further improve the effectiveness of the FTC mechanism under possible simultaneous actuator and sensor failures, similar to the FTC types (passive FTC and active FTC), there are also passive and active methods that can be applied to estimate unknown or inaccurate dynamic states. Marcello et al. presented a "passive" FTC design method using neural networks [15], where the fixed PFTC controller, based on pre-trained neural networks, can respond to inaccurate failure identification and sensor failures in the case of prior known faults. In a recent, neural-based strategy [18], aircraft outputs were constrained. Active methods include observer-based ones; for example, Lin et al. presented an observer-based networked control scheme to cope with the sensor delay problem [19]. To improve the output feedback controller performance, the authors integrated an observer link into the overall scheme to measure random sensor delays. Among the various observer-based methods, the fuzzy observer-based FTC scheme also has wide applications, such as nonlinear large-scale systems and so on [20,21].

Xiao et al. presented a sliding mode observer (SMO)-based method to reconfigure the FTC strategy to cope with actuator faults [22], where an SMO is used to measure system uncertainty. Li et al. presented an observer-based attitude control strategy for rigid aircraft [23], where the observer is also used to address model uncertainty. Yu et al. presented a sliding mode- and adaptive technique-based aircraft FTC strategy for simultaneous actuator and sensor fault conditions. The authors investigated the integrated design of SMO and FTC fight control, providing valuable results [24]. Except for system-level applications such as flight control models or actuation systems, the observer-based method can also be used in power electronic converters. For example, Xie et al. studied the diagnosis and resilient control problem for multiple sensor faults in cascaded H-bridge multi-level converters by using a reduced-order observer [25]. Xu et al. studied diagnosis problems for power switch, grid-side current sensor, and DC-link voltage sensor faults in single-phase three-level rectifiers [26]. Besides the observer-based FTC method, space vector modulation (SVM) can also be used in fault diagnoses and control problems [27]. These studies all focused on specific system failures. Compared with neural network- or SVM-based methods, the observer-based strategy is more widely used. However, this kind of scheme needs to be more flexible and able to cope with more complex and changing fault cases, even including cases where the numbers whereby degraded and/or failed actuators and sensors change over time [28]. The most important function of a designed observer is to provide equivalent states for a real system without false alarms. To solve this problem, Doostmohammadian and Charalambous analyzed the observational equivalence problem and proposed a Q-redundant observer design method using sensor networks [29]. The sensor-network-structure-based algorithm was able to recover sensor networks accurately with polynomial-order complexity.

For the NSV FTC problem, there is a considerable real-time requirement in performing the proposed algorithm; therefore, computational complexity should be avoided. Motivated by model-based monitoring and fault diagnosis methods, the NSV states can be estimated by using a similar concomitant system with the same original structure and input. In this

paper, a concomitant observer-based multi-level FTC strategy is proposed. First, under normal operating conditions, a fixed-structure observer is designed to estimate all the NSV states, and in the case when there are no sensor faults, the state feedback control law will use the original NSV states rather than the estimated observer states. However, if sensor failures occur, leading to some unknown NSV states, they can be estimated by implementing the concomitant observer, which can estimate the sensor failures caused unknown NSV states. This approach allows a hybrid state-feedback-based FTC law to be reconfigured by using the remaining normal NSV states and the corresponding concomitant observer states. In the case of additional sensor failures, the FTC law can be generated again to cope with the new faults by changing the observer dimension and structure. Consequently, since the unknown states caused by the sensor failures can be regenerated by the concomitant-observer, a new FTC law can be used for different actuator fault conditions. The linear quadratic regulator (LQR) technique is used to adjust the FTC gain [30].

Compared with previous works, the novelty of this paper is its use of a new FTC framework for NSV complex changing fault conditions. It contains three innovative elements: the NT-DRAS model in the NSV input link; a flexible concomitant observer for the real-time changing sensor fault conditions; and a multi-level FTC algorithm. The above elements are integrated as a schematism for NSVs. This has significant effects and advantages. Since the NT-DRAS is used in the NSV, in order to utilize the NT-DRAS dissimilar redundancy resources, different level FTC strategies (NT-DRAS level and flight control level) are performed to form a multi-level FTC mechanism. By using the proposed intelligent FTC mechanism described in this paper, NSVs can realize "never give up" FTC based on the fundamental channel reconfiguration when facing complex changing fault conditions, considering both NT-DRAS and sensor faults.

2. Problem Statement: NT-DRAS and Sensor Fault Modelling for NSVs

2.1. Baseline Control Model for NSVs under Normal Conditions

Figure 1 depicts a NSV conceptual design example.

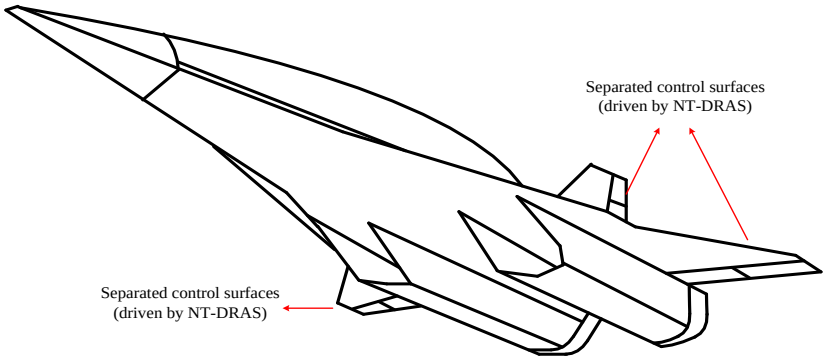


Figure 1. NSV conceptual design.

As shown in Figure 1, the NSV has separate control surfaces to provide sufficient redundancy in flight control levels and to assure the controllability of the NSV, even in cases whereby actuator faults occur. This paper addresses the condition whereby the NSV suffers from both NT-DRAS and sensor faults. As a control system, and using the state space method [31], the lateral-directional NSV model with configured NT-DRASs is shown in Equation (1):

$$\begin{cases} \dot{\boldsymbol{x}}(t) = \boldsymbol{A}_{\text{normal}}\boldsymbol{x}(t) + \boldsymbol{B}_{\text{normal}}\boldsymbol{u}(t) + \boldsymbol{G}\boldsymbol{w}(t) \\ \boldsymbol{y}(t) = \boldsymbol{C}_{\text{normal}}\boldsymbol{x}(t) \end{cases} \tag{1}$$

where $\boldsymbol{x} = \begin{bmatrix} \beta & p & r & \phi \end{bmatrix}^{\mathrm{T}}$ and in which β, p, r, ϕ are the sideslip angle, roll rate, yaw rate, and roll angle, respectively. The NSV model control inputs are provided by using the NT-DRASs as $\boldsymbol{u} = \begin{bmatrix} \delta_{\text{ain}}^{\text{NT-DRAS}} & \delta_{\text{aout}}^{\text{NT-DRAS}} & \delta_{\text{sp}}^{\text{NT-DRAS}} & \delta_{\text{rup}}^{\text{NT-DRAS}} & \delta_{\text{rlow}}^{\text{NT-DRAS}} \end{bmatrix}^{\mathrm{T}}$, in

which $\delta_{\text{ain}}^{\text{NT-DRAS}}$, $\delta_{\text{aout}}^{\text{NT-DRAS}}$, $\delta_{\text{sp}}^{\text{NT-DRAS}}$, $\delta_{\text{rup}}^{\text{NT-DRAS}}$, $\delta_{\text{rlow}}^{\text{NT-DRAS}}$ are the NT-DRAS-driving control surface deflections used in the inside and outside aileron, spoiler, and upper and lower rudder, respectively; $\boldsymbol{w}(t)$ is an uncontrollable disturbance, $\boldsymbol{y}(t)$ is the NSV output, and $\boldsymbol{A}_{\text{normal}}$, $\boldsymbol{B}_{\text{normal}}$, $\boldsymbol{C}_{\text{normal}}$, and $\boldsymbol{G}$ are the NSV system matrices representing state, input, output, and disturbance under normal conditions, respectively. The following assumptions are made when developing the proposed FTC strategy for NSVs under fault conditions.

Assumption 1 [14]. *Each control surface of the NSV is independent and driven by using a NT-DRAS. For the EHA and EMA channels of the NT-DRAS, both actuation efficiency degradation and complete channel failure are contingent.*

Assumption 2 [24]. *The NSV model is configured with sensors set for the sideslip and roll angles and the roll and yaw rates. It is assumed that the sensors are either in normal or complete failure states, since the sensors are used to collect the NSV states in signal form.*

Assumption 3 [7,28]. *In all of the studied fault cases, even when multiple NT-DRAS faults occur, there are at least the effective NT-DRAS channels corresponding with the fundamental flight control functions, which will still work. There are also sensors for the main states, which are normal. This is the hardware basis for the FTC design.*

Assumption 4 [14]. *For external disturbance$\boldsymbol{w}(t)$ effected on the NSV, though it is initially uncontrollable, it is assumed to be bounded and cannot cause the NSV output states to change sharply.*

Based on the above assumptions, the baseline controller for the NSV model under normal operating conditions can be determined. Figure 2 illustrates the baseline control scheme for the NSV model, in which there are NT-DRAS driven control surfaces providing inputs for the NSV model and corresponding sensors observing the NSV output states.

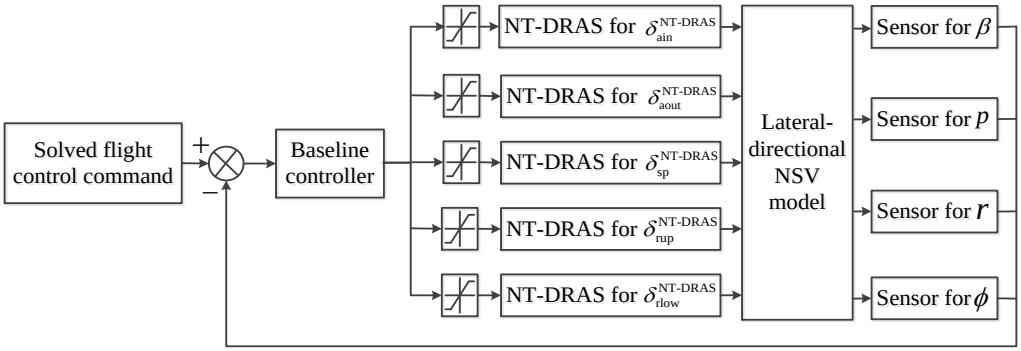


Figure 2. Baseline control scheme for the NSV model under normal operating conditions.

2.2. NT-DRAS Model and Fault Modelling in Flight Control Level

2.2.1. NT-DRAS Model

Figure 3 presents a NT-DRAS model with schematic and component information.

As described in [8] and shown in Figure 3, a NT-DRAS has two working channels, which are the EHA channel and the EMA channel. Each channel can drive the control surface independently and provide control input for the flight control level NSV model, leading to different operation modes. In this paper, a NT-DRAS can provide control input with two working channels, which can be modeled as follows:

$$\delta_{*}^{\text{NT-DRAS}} = f_{\text{switch}}^{\text{NT-DRAS}} \cdot \delta_{*}^{\text{EHA}} + (1 - f_{\text{switch}}^{\text{NT-DRAS}}) \cdot \delta_{*}^{\text{EMA}} \tag{2}$$

where $\delta_*^{\mathrm{NT-DRAS}}$ is the vector $\boldsymbol{u} = \left[\delta_{\mathrm{ain}}^{\mathrm{NT-DRAS}} \quad \delta_{\mathrm{aout}}^{\mathrm{NT-DRAS}} \quad \delta_{\mathrm{sp}}^{\mathrm{NT-DRAS}} \quad \delta_{\mathrm{rup}}^{\mathrm{NT-DRAS}} \quad \delta_{\mathrm{rlow}}^{\mathrm{NT-DRAS}}\right]^{\mathrm{T}}$ element, δ_*^{EHA} and δ_*^{EMA} are the EHA and EMA driven control surface deflection angles respectively, and $f_{\mathrm{switch}}^{\mathrm{NT-DRAS}}$ is the NT-DRAS channel switching function and can be defined as follows:

$$f_{\mathrm{switch}}^{\mathrm{NT-DRAS}} = \begin{cases} 1, & \mathrm{EHA}\ \ channel\ \ outputs \\ 1/2, & \mathrm{EHA}\ \ and\ \ \mathrm{EMA}\ \ output\ \ together \\ 0, & \mathrm{EMA}\ \ channel\ \ outputs \end{cases} \tag{3}$$

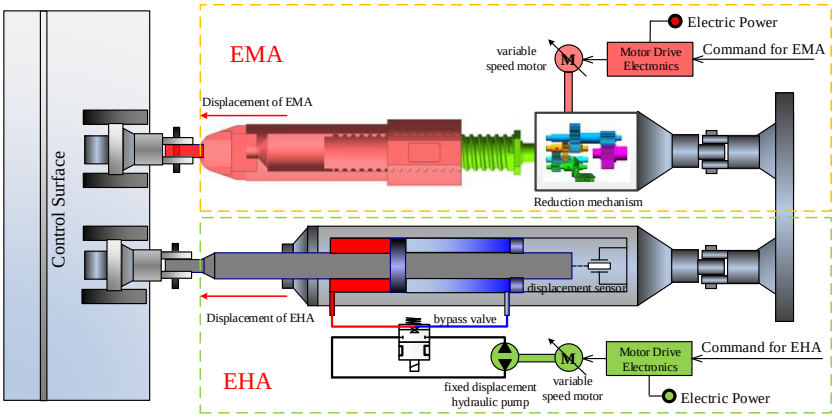


Figure 3. NT-DRAS model.

Remark 1. $f_{\mathrm{switch}}^{\mathrm{NT-DRAS}} = 1/2$ *represents the operation mode-3 studied in* [8,32]*, in which both the EHA and the EMA channel provide one half output force simultaneously without force fighting. This mode could be an alternative FTC choice when both the EHA and the EMA degrade but retain a certain level performance, or under certain conditions whereby the control surface has a high load.*

2.2.2. NT-DRAS Fault Modelling in Flight Control Level

The NSV control surfaces are driven by their related NT-DRASs. The NT-DRAS status can be defined using the following index matrix:

$$\boldsymbol{H}^{\mathrm{NT-DRAS}} = diag\left\{h_{\mathrm{ain}}^{\mathrm{NT-DRAS}} \quad h_{\mathrm{aout}}^{\mathrm{NT-DRAS}} \quad h_{\mathrm{sp}}^{\mathrm{NT-DRAS}} \quad h_{\mathrm{rup}}^{\mathrm{NT-DRAS}} \quad h_{\mathrm{rlow}}^{\mathrm{NT-DRAS}}\right\} \tag{4}$$

where $h_{\mathrm{ain}}^{\mathrm{NT-DRAS}}$, $h_{\mathrm{aout}}^{\mathrm{NT-DRAS}}$, $h_{\mathrm{sp}}^{\mathrm{NT-DRAS}}$, $h_{\mathrm{rup}}^{\mathrm{NT-DRAS}}$ and $h_{\mathrm{rlow}}^{\mathrm{NT-DRAS}}$ are the performance indices of the NSV corresponding control surfaces. The definition method in Equation (4) refers to the research described in [14]. Since the NT-DRAS dynamics can be ignored in the flight control level, only the transfer function gain is used to characterize the control action effectiveness. For one NT-DRAS working under a certain mode, the solved NT-DRAS deflection command $\delta_*^{\mathrm{command}}$ and the actual response $\delta_*^{\mathrm{NT-DRAS}}$ can have a transfer function relationship, i.e., $\delta_*^{\mathrm{NT-DRAS}}(s)/\delta_*^{\mathrm{command}}(s) = G_*^{\mathrm{NT-DRAS}}(s)$. Since the control signal can be described as $\delta_*^{\mathrm{NT-DRAS}}(t) = G_*^{\mathrm{NT-DRAS}} * \delta_*^{\mathrm{command}}(t)$ under no fault conditions, when faults occur, it can be described as $\delta_{*-\mathrm{fault}}^{\mathrm{NT-DRAS}}(t) = G_{*-\mathrm{fault}}^{\mathrm{NT-DRAS}} * \delta_*^{\mathrm{command}}(t)$; thus, the ratio between $\delta_{*-\mathrm{fault}}^{\mathrm{NT-DRAS}}$ and $\delta_*^{\mathrm{NT-DRAS}}$ essentially describes the effectiveness of the NT-DRAS.

According to Assumption 1, by defining variable $h_*^{\mathrm{NT-DRAS}}$, it can be determined that $\delta_{*-\mathrm{fault}}^{\mathrm{NT-DRAS}} = h_*^{\mathrm{NT-DRAS}} * \delta_*^{\mathrm{NT-DRAS}}$, where $h_*^{\mathrm{NT-DRAS}} = G_{*-\mathrm{fault}}^{\mathrm{NT-DRAS}}/G_*^{\mathrm{NT-DRAS}}$ and $0 \le h_*^{\mathrm{NT-DRAS}} \le 1$ is the NT-DRAS actuating effectiveness range. $h_*^{\mathrm{NT-DRAS}} = 1$ means that the NT-DRAS current working channel is in good condition, while $h_*^{\mathrm{NT-DRAS}} = 0$ means complete NT-DRAS failure. The values $0 < h_*^{\mathrm{NT-DRAS}} < 1$ can be used to describe performance degradation of the current NT-DRAS working channel. Similarly, with the definition in Equation (2), the common NT-DRAS health index function can be defined as:

$$h_*^{\mathrm{NT-DRAS}} = f_{\mathrm{switch}}^{\mathrm{NT-DRAS}} \cdot h_*^{\mathrm{EHA}} + (1 - f_{\mathrm{switch}}^{\mathrm{NT-DRAS}}) \cdot h_*^{\mathrm{EMA}} \tag{5}$$

where $h_*^{\mathrm{NT-DRAS}}$ represents the matrix elements in Equation (4) and h_*^{EHA} and h_*^{EMA} are the health state indices of the EHA channel and the EMA channel respectively. In order to model partial actuator faults, control input matrix $\boldsymbol{B}$ of the flight control NSV model should be updated as follows:

$$\boldsymbol{B}_{fault} = \boldsymbol{B}_{\mathrm{normal}} \boldsymbol{H}^{\mathrm{NT-DRAS}} \tag{6}$$

where $\boldsymbol{B}_{fault}$ is the NSV new input matrix under partial NT-DRASs fault conditions.

2.3. Sensors Fauls Modelling in Flight Control Level

NSV measurement output vector $\boldsymbol{y}(t)$ is obtained by the respective sensors. Similarly, with the modeling method in Equation (4), the sensor health status index vector can be determined as:

$$\boldsymbol{H}^{\mathrm{sensor}} = diag\left\{ h_\beta^{\mathrm{sensor}} \quad h_p^{\mathrm{sensor}} \quad h_r^{\mathrm{sensor}} \quad h_\phi^{\mathrm{sensor}} \right\} \tag{7}$$

where $h_\beta^{\mathrm{sensor}}$, h_p^{sensor}, h_r^{sensor}, and h_ϕ^{sensor} are the sensor health status indices of the corresponding four NSV measurement output states. As opposed to the NT-DRAS performance indices and according to Assumption 2, the index values are considered to be either 0 or 1 due to the sensor failure mechanism. Different from the common NT-DRAS health index function definition in Equation (5), the NSV sensor health index function can be defined as an event-trigger form with only values of 1 or 0:

$$h_*^{\mathrm{sensor}} = \begin{cases} 1, & sensor \;\; is \;\; in \;\; good \;\; condition; \\ 0, & sensor \;\; failed. \end{cases} \tag{8}$$

where h_*^{sensor} represents the matrix elements in Equation (7). In order to model the sensor fault, the output matrix $\boldsymbol{C}$ of the flight control NSV model should be updated as follows:

$$\boldsymbol{C}_{fault} = \boldsymbol{C}_{\mathrm{normal}} \boldsymbol{H}^{\mathrm{sensor}} \tag{9}$$

where $\boldsymbol{C}_{fault}$ is the NSV output matrix under sensor fault conditions.

2.4. The NSV Model under Comprehensive Fault Conditions

Since NT-DRAS and sensor faults are modeled using Equation (6) and Equation (9), respectively, the flight control level NSV model under comprehensive fault conditions can be modeled as:

$$\begin{cases} \dot{\boldsymbol{x}}(t) = \boldsymbol{A}_{\mathrm{normal}} \boldsymbol{x}(t) + \boldsymbol{B}_{fault} \boldsymbol{u}(t) + \boldsymbol{G} \boldsymbol{w}(t) \\ \boldsymbol{y}(t) = \boldsymbol{C}_{fault} \boldsymbol{x}(t) \end{cases} \tag{10}$$

3. Multi-Level Fault-Tolerant Control Strategy Development

3.1. Overall Architecture for the NSV FTC Problem

Figure 4 illustrates the NSV multi-level FTC mechanism, which contains NT-DRASs that have been set to cope with actuation system faults and a concomitant observer to cope with sensor system faults. These FTC resources are controlled and used via the proposed multi-level FTC algorithm.

As shown in Figure 4, all the actuators driving the control surfaces are in NT-DRAS form. If no fault occurs in the NSV model, the baseline controller is used for flight control. However, once faults or performance degradations occur in NT-DRASs and/or sensors, the fault detection and diagnosis (FDD) scheme can provide detailed fault information. The fault information can then be transmitted to the FTC decision mechanism, and the current controller can be switched from the baseline to the LQR form. In changing fault cases of the NT-DRASs and sensors, the proposed concomitant observer can observe the sensor failure caused unknown states and integrate those observation states with the remaining correct NSV measurement output states. The hybrid state integration scheme can then transmit the

new NSV states vector to the feedback closed loop, assuring that the reconfiguration control law can be generated successfully. The LQR controller FTC gain is obtained based on the FDD information, which can be solved by using the proposed reconfiguration algorithm. To maintain the desired NSV performance, the LQR-based FTC controller gains should be solved and adjusted online. Once the flight control level LQR-based FTC strategy cannot realize the desired flight performance, the faulty NT-DRAS can switch the fault working channel to the backup one, so that a necessary number of actuating channels can be used to support the LQR-based control gain adjustment.

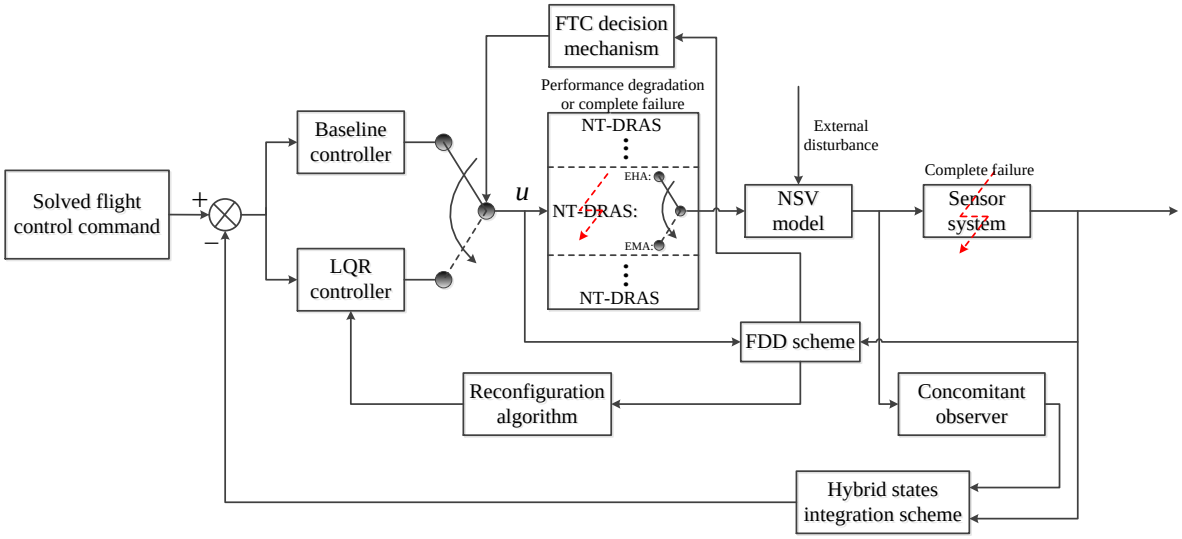


Figure 4. NSV multi-level FTC mechanism.

3.2. NSV Baseline Controller Structure

The NSV flight controller was designed with fixed structure. For a given flight control command, $\boldsymbol{r}_{\text{flight}}(t)$, and NSV output states $\boldsymbol{S}_{\text{out}}\boldsymbol{y}(t)$, the controller should guarantee the desired performance, i.e., $\lim_{t\to\infty} \boldsymbol{e}_{\text{track}}(t) = \boldsymbol{0}$, in which $\boldsymbol{e}_{\text{track}}(t) = \boldsymbol{r}_{\text{flight}}(t) - \boldsymbol{S}_{\text{out}}\boldsymbol{y}(t)$. The tracking performance can be optimized by using the function in Equation (13). The NSV augmented system is shown in Equation (11):

$$\begin{cases} \dot{\boldsymbol{x}}_{\text{aug}}(t) = \boldsymbol{A}_{\text{aug}}\boldsymbol{x}_{\text{aug}}(t) + \boldsymbol{B}_{\text{aug}}\boldsymbol{u}(t) + \boldsymbol{G}_{\text{aug}}\boldsymbol{w}_{\text{aug}}(t) \\ \boldsymbol{y}_{\text{aug}}(t) = \boldsymbol{C}_{\text{aug}}\boldsymbol{x}_{\text{aug}}(t) \end{cases} \tag{11}$$

where $\boldsymbol{x}_{\text{aug}}(t) = \begin{bmatrix} \boldsymbol{x}(t) & \int \boldsymbol{e}_{\text{track}}(t)\boldsymbol{dt} \end{bmatrix}^{\text{T}}$ and $\boldsymbol{y}_{\text{aug}}(t) = \begin{bmatrix} \boldsymbol{y}(t) & \int \boldsymbol{e}_{\text{track}}(t)\boldsymbol{dt} \end{bmatrix}^{\text{T}}$ are the augmented state and output vector, respectively, and $\boldsymbol{w}_{\text{aug}}(t) = \begin{bmatrix} \boldsymbol{w}(t) & \boldsymbol{r}_{\text{flight}}(t) \end{bmatrix}^{\text{T}}$ is the augmented disturbance vector. Other augmented matrices are given as $\boldsymbol{A}_{\text{aug}} = \begin{bmatrix} \boldsymbol{A}_{\text{normal}} & \boldsymbol{0} \\ -\boldsymbol{S}_{\text{out}}\boldsymbol{C}_{\text{normal}} & \boldsymbol{0} \end{bmatrix}$, $\boldsymbol{B}_{\text{aug}} = \begin{bmatrix} \boldsymbol{B}_{fault} \\ \boldsymbol{0} \end{bmatrix}$, $\boldsymbol{C}_{\text{aug}} = \begin{bmatrix} \boldsymbol{C}_{fault} & \boldsymbol{0} \\ \boldsymbol{0} & \boldsymbol{I} \end{bmatrix}$, and $\boldsymbol{G}_{\text{aug}} = \begin{bmatrix} \boldsymbol{G} & \boldsymbol{0} \\ \boldsymbol{0} & \boldsymbol{I} \end{bmatrix}$.

The controller was designed similarly to the one in [7,14], with the state and output error integration feedback form in Equation (12), which guarantees the NSV flight control tracking performance, i.e.,

$$\boldsymbol{u}(t) = \boldsymbol{K}_{flight}\boldsymbol{x}_{\text{aug}}(t) = \boldsymbol{K}_{\boldsymbol{x}}\boldsymbol{x}(t) + \boldsymbol{K}_{\text{e}}\int_0^t \boldsymbol{e}_{\text{track}}(\tau)d\tau \tag{12}$$

where matrix $\boldsymbol{K}_{flight} = \begin{bmatrix} \boldsymbol{K}_{\boldsymbol{x}} & \boldsymbol{K}_{\boldsymbol{e}} \end{bmatrix}$ is the solved controller gain for the NSV model. To optimize the NSV control performance, linear-quadratic (LQ) quantization function $\boldsymbol{J}_{\text{LQ}}$, used to evaluate the flight quality, is defined as:

$$\boldsymbol{J}_{\mathrm{LQ}} = \int_0^t \left(\boldsymbol{x}_{\mathrm{aug}}^{\mathrm{T}}(\tau)\boldsymbol{Q}\boldsymbol{x}_{\mathrm{aug}}(\tau) + \boldsymbol{u}(\tau)^{\mathrm{T}}\boldsymbol{R}\boldsymbol{u}(\tau) \right) d\tau \tag{13}$$

where $\boldsymbol{Q}$ and $\boldsymbol{R}$ are symmetric positive semi-definite and positive definite weighting matrices, respectively. NSVs can achieve better performance when $\boldsymbol{J}_{\mathrm{LQ}}$ is optimized and calculated as a smaller value [7,14].

3.3. Concomitant Observer Design

As a virtual system of the NSV model, the concomitant observer to be designed should guarantee that all the virtual states can converge to the real system states. Therefore, the full state observer form is essentially a concomitant observer under normal conditions. Considering both the state feedback control law in Equation (12) and the NSV model in Equation (10), the following new NSV model form can be derived:

$$\begin{cases} \dot{\boldsymbol{x}}(t) = \boldsymbol{A}_{\mathrm{normal}}\boldsymbol{x}(t) + \boldsymbol{B}_{fault}\boldsymbol{K}_{\boldsymbol{x}}\boldsymbol{x}(t) + \boldsymbol{B}_{fault}\boldsymbol{K}_{\boldsymbol{e}}\int_0^t \boldsymbol{e}_{\mathrm{track}}(\tau)d\tau + \boldsymbol{G}\boldsymbol{\omega}(t) \\ \boldsymbol{y}(t) = \boldsymbol{C}_{fault}\boldsymbol{x}(t) \end{cases} \tag{14}$$

The baseline concomitant observer form with its full states can be given as:

$$\begin{cases} \dot{\tilde{\boldsymbol{x}}}(t) = \boldsymbol{A}_{\mathrm{normal}}\tilde{\boldsymbol{x}}(t) + \boldsymbol{B}_{fault}\boldsymbol{K}_{\tilde{\boldsymbol{x}}}\tilde{\boldsymbol{x}}(t) + \boldsymbol{B}_{fault}\boldsymbol{K}_{\boldsymbol{e}}\int_0^t \boldsymbol{e}_{\mathrm{track}}(\tau)d\tau + \boldsymbol{L}_{\mathrm{ob}}\boldsymbol{C}_{fault}\left(\boldsymbol{x}(t) - \tilde{\boldsymbol{x}}(t)\right) \\ \tilde{\boldsymbol{y}}(t) = \boldsymbol{C}_{fault}\tilde{\boldsymbol{x}}(t) \end{cases} \tag{15}$$

where $\boldsymbol{L}_{\mathrm{ob}}$ is the concomitant observer gain to be solved, and $\tilde{\boldsymbol{x}} = \begin{bmatrix} \beta_{\mathrm{ob}} & p_{\mathrm{ob}} & r_{\mathrm{ob}} & \phi_{\mathrm{ob}} \end{bmatrix}^{\mathrm{T}}$ is the observer state vector. If no fault occurs in the sensor system, the control input for the NSV model can be generated as in Equation (12). However, if the sensor faults occur in the NSV model, the concomitant observer should implement the sensor failure caused unknown states, so that hybrid state vector $\boldsymbol{x}_{\mathrm{hybrid}}$ can be used to generate the NSV control input law, which is shown in Equation (16).

$$\boldsymbol{u}(t) = \boldsymbol{K}_{\boldsymbol{x}}\boldsymbol{x}_{\mathrm{hybrid}}(t) + \boldsymbol{K}_{\boldsymbol{e}}\int_0^t \boldsymbol{e}_{\mathrm{track}}(\tau)d\tau \tag{16}$$

To assure the convergence between the concomitant observer and the NSV model, the following error dynamic system is given first in Equation (17), and then the error dynamic system matrices can be used to solve the original concomitant observer gain by using the LMI technique:

$$\begin{aligned} \dot{\tilde{\boldsymbol{e}}}_{\mathrm{ob}}(t) &= \dot{\boldsymbol{x}}(t) - \dot{\tilde{\boldsymbol{x}}}(t) \\ &= \boldsymbol{A}_{\mathrm{normal}}\boldsymbol{x}(t) + \boldsymbol{B}_{fault}\boldsymbol{K}_{\boldsymbol{x}}\boldsymbol{x}_{\mathrm{hybrid}}(t) + \boldsymbol{B}_{fault}\boldsymbol{K}_{\boldsymbol{e}}\int_0^t \boldsymbol{e}_{\mathrm{track}}(\tau)d\tau + \boldsymbol{G}\boldsymbol{\omega}(t) \\ &\quad -\boldsymbol{A}_{\mathrm{normal}}\tilde{\boldsymbol{x}}(t) - \boldsymbol{B}_{fault}\boldsymbol{K}_{\boldsymbol{x}}\boldsymbol{x}_{\mathrm{hybrid}}(t) - \boldsymbol{B}_{fault}\boldsymbol{K}_{\boldsymbol{e}}\int_0^t \boldsymbol{e}_{\mathrm{track}}(\tau)d\tau - \boldsymbol{L}_{\mathrm{ob}}\boldsymbol{C}_{fault}\left(\boldsymbol{x}(t) - \tilde{\boldsymbol{x}}(t)\right) \\ &= \left(\boldsymbol{A}_{\mathrm{normal}} - \boldsymbol{L}_{\mathrm{ob}}\boldsymbol{C}_{fault}\right)\tilde{\boldsymbol{e}}_{\mathrm{ob}}(t) + \boldsymbol{G}\boldsymbol{\omega}(t) \end{aligned} \tag{17}$$

Theorem 1. *Considering the closed-loop system with unknown output states in Equation (14), by defining its initial concomitant observer form in Equation (15), for a given attenuation level scalar* γ_{ob}**>**0*, if there is a symmetric positive definite matrix, i.e.,* $\boldsymbol{P}_{\mathrm{ob}} = \boldsymbol{X}_{\mathrm{ob}}^{-1}$*, and other adaptation matrices form* $\boldsymbol{V}_{\mathrm{ob}}$*,* $\boldsymbol{N}_{\mathrm{ob}}$*, and* $\boldsymbol{M}_{\mathrm{ob}}$*, such that the LMI form (A5) can hold, then the concomitant observer gain matrix can be solved as* $\boldsymbol{L}_{\mathrm{solved}} = \boldsymbol{N}_{\mathrm{ob}}\boldsymbol{V}_{\mathrm{ob}}^{-1}\boldsymbol{C}_{fault}^{-1}$*, where* $\boldsymbol{C}_{fault}^{-1}$*is in pseudo-inverse form.*

For Proof of Theorem 1, see Appendix A.

Remark 2. *In Theorem 1, the resulting matrix, $\boldsymbol{L}_{\text{solved}}$, can guarantee the concomitant observer convergence. By defining adjustment coefficient ρ_{ob}, and choosing the actual applied observer gain form $\boldsymbol{L}_{\text{used}} = \rho_{\text{ob}}\boldsymbol{L}_{\text{solved}}$, then the observer can achieve the desired convergence efficiency.*

3.4. Determination of Concomitant Observer-Based FTC Gain

The function of the designed concomitant observer is that it can map the real NSV model states in a timely manner and provide the missing unknown states, since it is concomitant with the real NSV model. Therefore, even under sensor fault conditions, the FTC gain can still be solved based on both the observer and real system hybrid states. To maintain the desired FTC performance, FTC gain $\boldsymbol{K_x}$ and $\boldsymbol{K_e}$ can be obtained by solving the following Riccati Equation [33]:

$$\boldsymbol{P}_{\text{RE}}\boldsymbol{A}_{\text{aug}} + \boldsymbol{A}_{\text{aug}}^{\text{T}}\boldsymbol{P}_{\text{RE}} - \boldsymbol{P}_{\text{RE}}\boldsymbol{B}_{\text{aug}}\boldsymbol{R}^{-1}\boldsymbol{B}_{\text{aug}}^{\text{T}}\boldsymbol{P}_{\text{RE}} + \boldsymbol{Q} = 0 \tag{18}$$

where $\boldsymbol{P}_{\text{RE}}$ is a definite and positive Riccati Equation matrix to be solved. The FTC gain can have the following form by solving Equation (18) using the LQR technique [30,33]

$$\begin{bmatrix}\boldsymbol{K_x}, & \boldsymbol{K_e}\end{bmatrix} = -\boldsymbol{R}^{-1}\boldsymbol{B}_{\text{aug}}^{\text{T}}\boldsymbol{P}_{\text{RE}} \tag{19}$$

Theorem 2. *Considering the augmented closed-loop system in Equation (11), for a given scalar, γ_{c}>0, for all nonzero disturbances, i.e., $\boldsymbol{w}(t) \in \boldsymbol{L}_2[0,\infty)$, $\boldsymbol{Q}$ and $\boldsymbol{R}$ are the chosen weighting matrices used in LQ index in Equation (13). If there is a symmetric positive definite matrix, i.e., $\boldsymbol{P}_{\text{RE}}$, such that the Riccati Equation form in Equation (18) can hold, then the augmented closed-loop system in Equation (11) can obtain the upper bound of performance index:*

$$\boldsymbol{J}_{\text{LQ}} < \boldsymbol{x}_{\text{aug}}^{\text{T}}(0)\boldsymbol{P}_{\text{c}}\boldsymbol{x}_{\text{aug}}(0) + \gamma_{\text{c}}^2\int_0^t \boldsymbol{w}_{\text{aug}}^{\text{T}}(\tau)\boldsymbol{w}_{\text{aug}}(\tau)d\tau \tag{20}$$

The FTC controller gain can be solved using the LQR technique, as $\begin{bmatrix}\boldsymbol{K_x}, & \boldsymbol{K_e}\end{bmatrix} = -\boldsymbol{R}^{-1}\boldsymbol{B}_{\text{aug}}^{\text{T}}\boldsymbol{P}_{\text{RE}}$.

For Proof of Theorem 2, see Appendix B.

Remark 3. *To realize smooth switching from the baseline controller to the LQR one, or from a former LQR gain to another due to changes in the fault case, the switching process can be defined by function $\boldsymbol{K}_{\text{now}}(t) = \boldsymbol{K}_{\text{now}}(t_0) + (\boldsymbol{K}_{\text{former}}(t_0) - \boldsymbol{K}_{\text{now}}(t_0))e^{-\tau(t-t_0)}$, where $\boldsymbol{K}_{\text{forner}}$ is the anterior control gain and $\boldsymbol{K}_{\text{now}}$ is the new FTC gain. The beginning switching time point is t_0 and τ; this depends on the NSV dynamic response. This method is similar to the switching method presented in* [14].

3.5. Multi-Level Reconfiguration FTC Algorithm under Fault Changing Cases

Figure 5 illustrates a flow chart of the concomitant observer-based multi-level FTC algorithm. The main strategies and branches to respond to different fault cases are introduced. Algorithm 1 presents the specific variables and criteria in the real-time FTC process. The NSV flight quality can be quantized using cost function $\boldsymbol{J}_{\text{LQ}}(t)$ in Equation (13). By setting a moving window length (calculating step) and a desired admissible flight quality value $\boldsymbol{J}_{\text{LQ}}^{\max}$, the NSV flight quality can be monitored in real time. Once the monitored $\boldsymbol{J}_{\text{LQ}}(t) > \boldsymbol{J}_{\text{LQ}}^{\max}$, the FTC mechanism can be triggered. In this paper, the Matlab/Simulink software was chosen as the algorithm computing and simulation platform. In the real NSV, the proposed algorithm can be migrated to the flight control computer system, which should process real-time data quickly and run the algorithm with high efficiency.

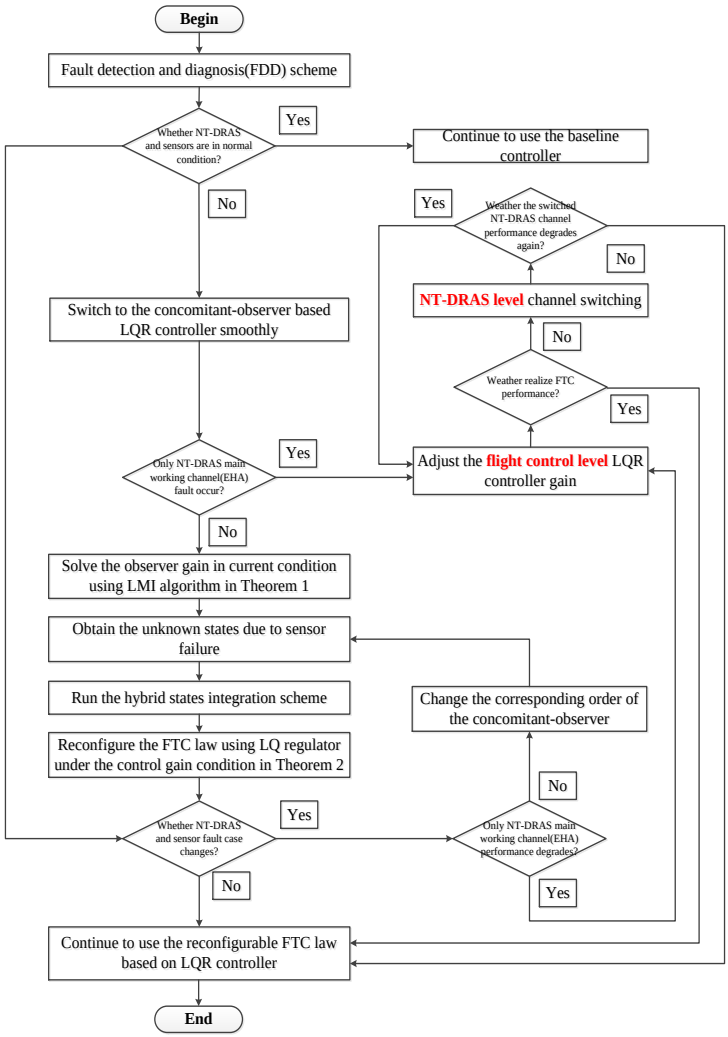


Figure 5. Flow chart of the concomitant observer-based multi-level FTC algorithm.

Algorithm 1: Concomitant observer-based multi-level FTC algorithm for the NSV with NT-DRASs

Step-1 **Input and Initialize:** **matrices** A_{normal}, B_{normal}, C_{normal}, G, $H^{\text{NT-DRAS}}$, H^{sensor}, and $J_{\text{LQ}}^{\max}$.

Step-2 Calculate $K_{\text{Case}-1}^{\text{base}}$ using **Theorem 2** to stabilize the NSV model and then measure the index $J_{\text{LQ}}(t)$ via Equation (13).

Step-3

if: $J_{\text{LQ}}(t) \leq J_{\text{LQ}}^{\max}$

Continue use the baseline controller;

else:

Update $H^{\text{NT-DRAS}}$ and H^{sensor} by using the FDD scheme;

if: $H^{\text{NT-DRAS}} \neq I$ (fault occurs in NT-DRASs) and $H^{\text{sensor}} = I$ (no fault in the NSV state sensor);

Calculate $K_{\text{Case}-\text{i}}^{\text{FTC}}$ by using LQR (algorithm in **Theorem 2**) as the new flight control gain and then recalculate $J_{\text{LQ}}(t)$ after a moving window period;

if: $J_{\text{LQ}}(t) \leq J_{\text{LQ}}^{\max}$

Continue use the LQR solved FTC control gain;

else:

Perform the NT-DRAS level channel switching for the detected faulty NT-DRASs;

end;

else if: $H^{\text{NT-DRAS}} = I$ (no fault in NT-DRASs) and $H^{\text{sensor}} \neq I$ (fault occurs in the sensors);

Calculate $L_{\text{solved}} = N_{\text{ob}} V_{\text{ob}}^{-1} C_{fault}^{-1}$ using **Theorem 1** and update $C_{fault} = C_{\text{normal}} H^{\text{sensor}}$;

Reconfigure the state-based feedback control law using the form in Equation (16);

else if: $H^{\text{NT-DRAS}} \neq I$ (fault occurs in NT-DRASs) and $H^{\text{sensor}} \neq I$ (fault occurs in sensors);

Calculate $L_{\text{solved}} = N_{\text{ob}} V_{\text{ob}}^{-1} C_{fault}^{-1}$ by using **Theorem 1** and updated $C_{fault} = C_{\text{normal}} H^{\text{sensor}}$;

Reconfigure the state-based feedback control law by using the form in Equation (16);
Calculate $\boldsymbol{K}_{\text{Case}-\text{i}}^{\text{FTC}}$ using LQR (algorithm in **Theorem 2**) as the new flight control gain and then recalculate $\boldsymbol{J}_{\text{LQ}}(t)$ after a moving window period;
if: $\boldsymbol{J}_{\text{LQ}}(t) \leq \boldsymbol{J}_{\text{LQ}}^{\max}$
Continue to use the LQR solved FTC control gain and the current concomitant observer gain;
else:
Perform the NT-DRAS level channel switching for the detected NT-DRAS fault;
end;
end;
end;
Step-4 **Return Step-2.**

As shown in Figure 5, the NT-DRASs and sensors fault information can be obtained by using the FDD scheme. The baseline controller is used when all the NT-DRASs and sensors are in fault-free conditions. Once a fault occurs, it can be smoothly switched to the concomitant observer-based one. If performance degradations or even total failure occur in the partial NT-DRAS main channels (EHA channel) while there are no sensor faults, then the LQR controller gain is adjusted to adapt to the current fault condition first. If the desired FTC performance cannot be realized, NT-DRAS channel switching should be performed, so that the NT-DRAS health state can be updated by using a new EMA channel. If the EMA channel continues to degrade, another circle LQR controller gain adjustment should be performed at the flight control level. If the system also experiences sensor faults, then the concomitant observer gain matrix for the current case can be determined, and the sensor failure caused unknown states can be estimated. By using the integration scheme, all the necessary states used to reconfigure the FTC law are available. The FTC law can then be determined following Theorem 2. If the fault case does not change, the NSV can maintain the current FTC law, but if the NT-DRAS channel fault conditions change, then continue to adjust the LQR controller gain directly. However, if the sensor fault case also changes, the concomitant observer should switch to a new concomitant status to obtain the new changed uncertain states. The measures to be taken will be the same as when determining the original reconfigurable FTC law. The proposed FTC method for complex changing cases can maintain NSV system stability, which is given as a theorem below.

Statement 1. *For the NSV augmented model in Equation (11) with subjected random disturbance form* $\boldsymbol{w}(t) \in \boldsymbol{L}_2[0, \infty)$*, i.e., multiple NT-DRAS and sensor changing fault conditions, by using the observer gain solved in Theorem 1 and the LQR control gain solved in Theorem 2, and performing the multi-level FTC algorithm in Figure 5, the NSV augmented model in Equation (11) can be stabilized, maintaining the performance described in Equation (20).*

For Proof of Statement 1, see Appendix C.

Remark 4. *In order to compare and quantize the NSV flight control tracking performance, similarly with the index form in* [14]*, a criterion function is given as* $e_{\text{perf}}(t) = \left\| r_{\text{flight}}(t) - y(t) \right\|_2$*, where* $r_{\text{flight}}(t)$ *is the given reference flight control command, and* $y(t)$ *is the NSV output response. In order to measure the conservatism of the NSV output states under different fault conditions, the mean and maximum values of* $e_{\text{perf}}(t)$ *are also defined in Equation (21) and used as the overall performance measures.*

$$\begin{cases} \bar{e}_{\text{perf}}(t) = \frac{1}{t_2 - t_1} \int_{t_1}^{t_2} e_{\text{perf}}(t) dt \\ e_{\text{perf}-\max} = \max\left\{ e_{\text{perf}}(t), t \in [t_1, t_2] \right\} \end{cases} \tag{21}$$

4. Case Studies and Simulations

To present the results well, the sequence of the subsection settings are first given a specification. Section 4.1 presents the NSV model data and baseline control gain under normal conditions. Section 4.2 presents the NSV fault scenario set, from Case 1 to

Case 4, as the NSV fault severity worsens, which can be exhibited in the simulation results of both the NSV and actuation system responses, respectively. Section 4.3 presents the LQR controller-based FTC results without considering the sensors faults, in which Section 4.3.1 illustrates the LQR-based FTC mechanism, Sections 4.3.2 and 4.3.3 illustrate different levels of FTC effectiveness, and Section 4.3.4 analyzes a sequence of different level FTC strategies. To further cope with sensors faults, an observer should be designed; therefore, Section 4.4 presents the proposed observer solved gain and the convergence results. Section 4.5 presents the final and most important findings about the comprehensive actuator system and sensor system changing fault conditions. Section 4.5.1 presents three different control strategies, Section 4.5.2 illustrates the compared results of S-1 and S-3. Finally, Section 4.5.3 illustrates the final compared results of S-2 and S-3 under different fault conditions, including a specific step signal tracking process and worsening comprehensive fault conditions, presenting the advantages of the proposed concomitant observer-based multi-level FTC algorithm.

4.1. System Model Matrices and Solved Baseline Control Gains

To perform simulation studies, the data are from a NASA GTM model [34]. Under normal conditions, the model matrices are given as:

$$\begin{cases} \boldsymbol{A}_{\text{normal}} = \begin{bmatrix} -0.0558 & 0.0802 & -0.9968 & 0.0415 \\ -3.0500 & -0.4650 & 0.3880 & 0 \\ 0.5980 & -0.0316 & -0.1150 & 0 \\ 0 & 1 & 0.0804 & 0 \end{bmatrix} \\ \boldsymbol{B}_{\text{normal}} = \begin{bmatrix} 0 & 0 & 0 & 0.0041 & 0.0032 \\ 0.268 & 0.3575 & 0.4469 & 0.126 & 0.027 \\ 0.0154 & 0.0193 & 0.0241 & -0.275 & -0.2 \\ 0 & 0 & 0 & 0 & 0 \end{bmatrix} \end{cases} \tag{22}$$

Under normal conditions, each NT-DRAS drives its corresponding control surface by using an EHA channel. All the working channels of the NSV are in good condition; therefore, the performance status matrix has the value $\boldsymbol{H}_{\text{Case}-1}^{\text{NT}-\text{DRAS}} = diag\{1 \quad 1 \quad 1 \quad 1 \quad 1\}$. The sensor system is also in a fault-free condition; therefore, the sensor system states matrix has the value $\boldsymbol{H}_{\text{Case}-1}^{\text{semsor}} = diag\{1 \quad 1 \quad 1 \quad 1\}$. By using the proposed algorithm in Theorem 1 and the LQR function in Matlab toolbox, the baseline control law can be solved as in Equation (23):

$$\boldsymbol{K}_{\text{Case}-1}^{\text{base}} = \begin{bmatrix} -4.5401 & 14.7867 & 3.0572 & 25.0202 & -14.0972 & 0.9487 \\ -5.6873 & 18.4836 & 3.8280 & 31.2763 & -17.6222 & 1.1906 \\ -7.1031 & 23.1056 & 4.7818 & 39.0970 & -22.0286 & 1.4858 \\ 79.7154 & 5.4810 & -36.6400 & 5.3639 & -2.2908 & -30.7376 \\ 5.8845 & 0.0658 & -2.6934 & -0.1683 & 0.1479 & -2.2511 \end{bmatrix} \tag{23}$$

4.2. NSV Fault Scenario Set

The NSV fault case scenarios are provided in Table 1. The complete failure and performance degradations are studied in [14]. In Case 1, all the NT-DRASs and sensors are in fault-free condition. In cases-2–4, complex changing fault cases occur, since both the current NT-DRAS working channels and sensor system suffer from performance degradation and/or failures. The fault scenarios are set to gradually deteriorate, which can be seen in performance status matrices $\boldsymbol{H}_{\text{Case}-\text{i}}^{\text{NT}-\text{DRAS}}$ and $\boldsymbol{H}_{\text{Case}-\text{i}}^{\text{semsor}}$.

Table 1. NSV fault case scenarios with health status matrices.

Case No.	NT−DRASs Performance Status Matrix $H_{Case-i}^{NT-DRAS}$	Sensors States Matrix H_{Case-i}^{semsor}
1	$H_{Case-1}^{NT-DRAS} = diag\{1 \quad 1 \quad 1 \quad 1 \quad 1\}$	$H_{Case-1}^{semsor} = diag\{1 \quad 1 \quad 1 \quad 1\}$
2	$H_{Case-2}^{NT-DRAS} = diag\{0 \quad 1 \quad 0.6 \quad 1 \quad 0\}$	$H_{Case-2}^{semsor} = diag\{1 \quad 0 \quad 1 \quad 1\}$
3	$H_{Case-3}^{NT-DRAS} = diag\{0 \quad 0.52 \quad 0.6 \quad 0.43 \quad 0\}$	$H_{Case-3}^{semsor} = diag\{1 \quad 0 \quad 0 \quad 1\}$
4	$H_{Case-4}^{NT-DRAS} = diag\{0 \quad 0.11 \quad 0.23 \quad 0.17 \quad 0\}$	$H_{Case-4}^{semsor} = diag\{1 \quad 0 \quad 0 \quad 0\}$

Figure 6 shows the NSV roll action response under different fault cases, in which a step reference signal with 12° amplitude in roll angle is given as the NSV solved command.

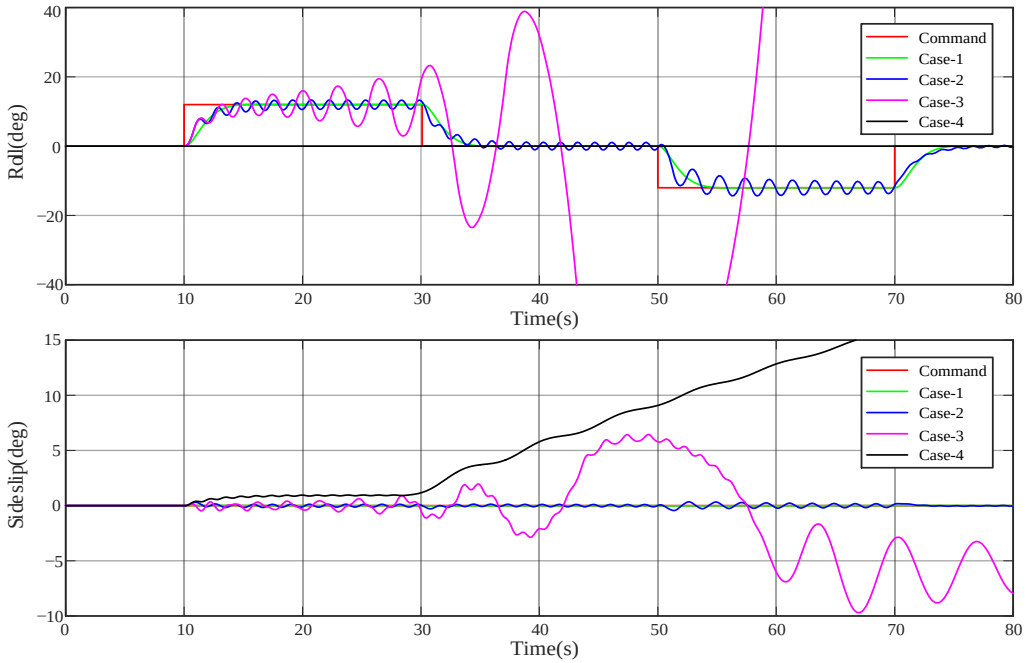


Figure 6. Roll and sideslip tracking responses using the baseline controller gain.

As shown in the four cases in Figure 6, the baseline controller under normal conditions is considered first. The original control gain, K_{Case-1}^{base} is determined and applied to simulate the system's dynamic responses. In Case 1, the given reference roll angle can be closely tracked with very small sideslip angle oscillation. In Cases 2–4 the two NSV output states diverge with increasing severity of the conditions, which indicates that the sensor failure is a fatal failure for the NSV and needs to be compensated for by effective FTC strategies. Meanwhile, the FTC controller should be designed to effectively reconfigure the comprehensive control gain under complex changing fault conditions.

Figure 7 illustrates the responses of all the NT-DRAS current channels under comprehensive fault conditions.

As shown in Figure 7, under normal conditions (Case 1), all control surfaces can undergo normal deflections. However, in Cases 2–4, it can be seen that due to abnormal outputs from the NSV model attitude, the calculated input of the NT-DRAS current channels continuously fluctuate within the saturation angle range, or even in a saturated actuating state.

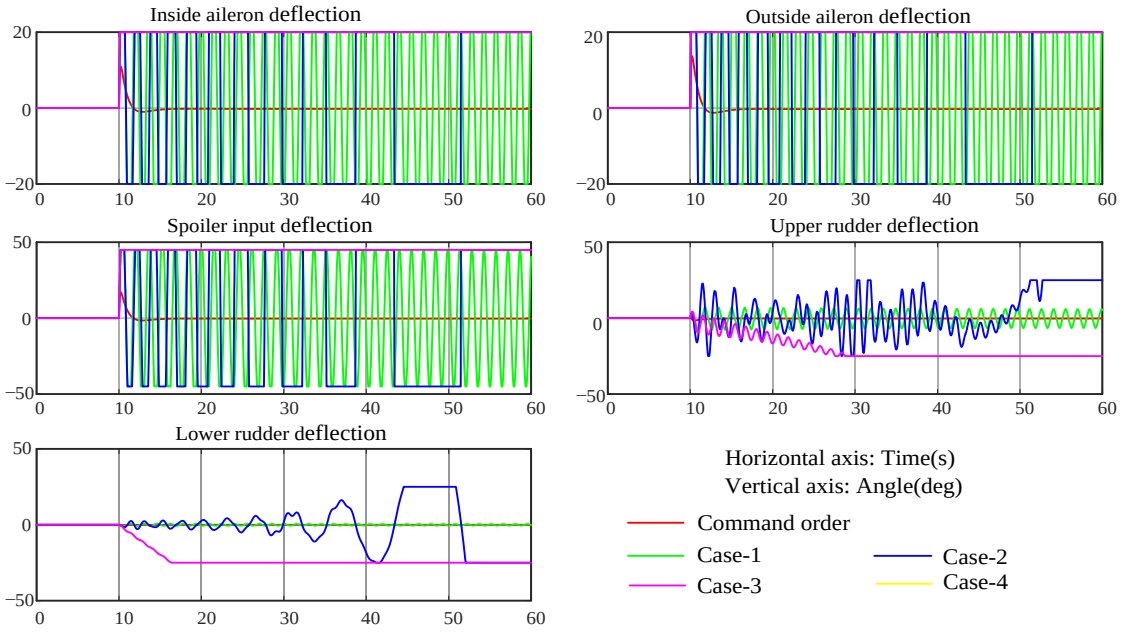


Figure 7. All NT-DRASs responses under comprehensive fault conditions.

4.3. Effectiveness Verification of LQR-Based FTC Controller for the NT-DRAS Faults

4.3.1. LQR Solved FTC Control Gain

When the NSV suffers from multiple NT-DRAS current working channels faults, controller switching would be performed to maintain a certain level of flight control performance. The original NT-DRAS fault condition is considered as Case 2, in which the corresponding lower rudder and inside aileron NT-DRAS channels have completely failed, and the performance of the corresponding spoiler NT-DRAS channel degrades to 60%. Under this condition, the LQR-based FTC gain can be solved using Equation (24).

$$\boldsymbol{K}_{\mathrm{Case-2}}^{\mathrm{FTC}} = \begin{bmatrix} 0 & 0 & 0 & 0 & 0 & 0 \\ -11.4211 & 26.9907 & 6.8689 & 45.1800 & -25.1893 & 2.3419 \\ -8.5622 & 20.2440 & 5.1498 & 33.8864 & -18.8927 & 1.7550 \\ 81.8157 & 6.1322 & -37.7248 & 6.4450 & -2.9265 & -31.4871 \\ 0 & 0 & 0 & 0 & 0 & 0 \end{bmatrix} \tag{24}$$

Figure 8 shows a comparison of the results for the NSV control surface deflections under Case 1 and Case 2.

As indicated in Figure 8, the NT-DRASs corresponding to the inside aileron and the lower rudder working channels have completely failed, resulting in no responses during the time range. The reconfigurable FTC gain matrix in Equation (24) shows that the control gains for the outside aileron and the upper rudder have increased, resulting in increased response magnitudes, ultimately compensating for failures caused by the failed NT-DRAS current channels. Although there is performance degradation in the corresponding spoiler NT-DRAS current channel, it still can achieve the desired response with the increased FTC gains.

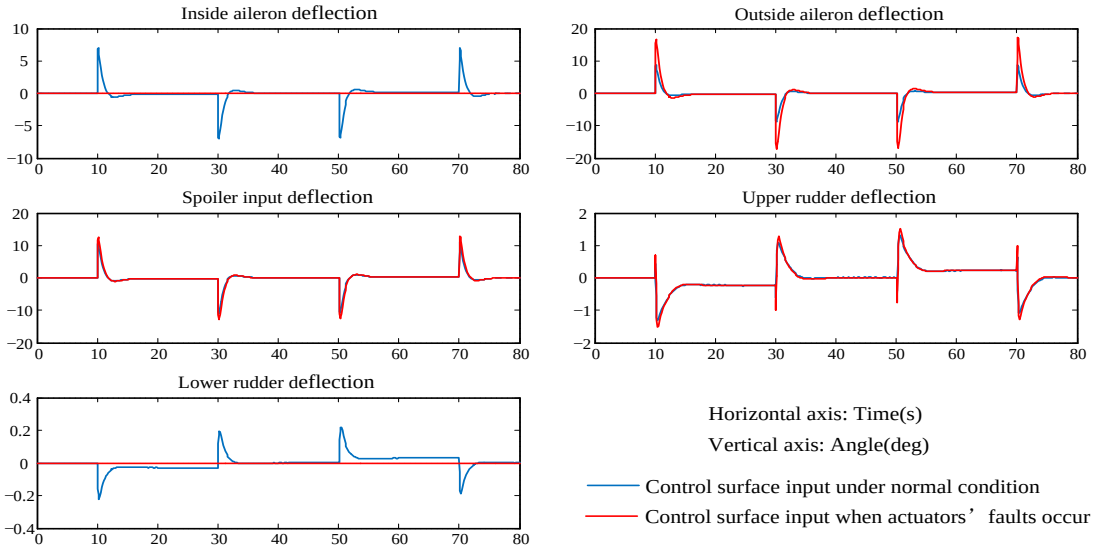


Figure 8. Comparison for the NSV control surface deflections under Case 1 and Case 2.

4.3.2. NT-DRAS Level-Based FTC Effectiveness Simulation

Figure 9 shows the comparison results of the NT-DRAS level-based FTC effectiveness, so that the FTC improvement of the NT-DRAS channel switching can be presented.

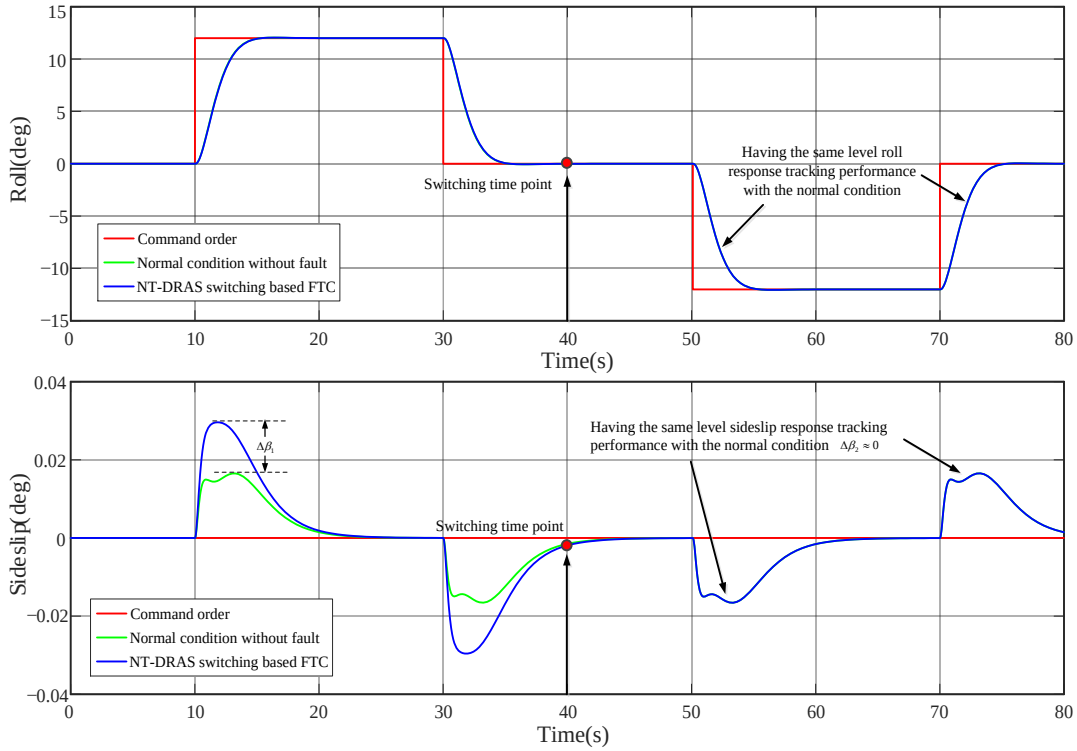


Figure 9. Comparison of actuation system level FTC effectiveness based on NT-DRAS.

As shown in Figure 9, the switching strategy here involves mitigating the performance degradation or complete failure of the current EHA channel by switching to the EMA channel. The switching occurs in the 40th second. From the response of the roll and sideslip angles at the flight control level, it is evident that after the switching, the roll angle fits the normal condition curve completely. Before the channel switching of the NT-DRAS, the sideslip angle of the NSV model increases by approximately $\Delta\beta_1 \approx 0.02^\circ$ during the roll motion compared with the normal condition. However, after the NT-DRAS switching

in the 40th second, it fully restores to the quality of normal condition, i.e., $\Delta\beta_2 \approx 0°$, as the EMA channel completely replaces the previously failed or degraded EHA channel. Consequently, both the roll and sideslip responses can reach a normal condition level.

4.3.3. Flight Control Level-Based FTC Effectiveness Simulation

Figure 10 shows a comparison of the results of the flight control level-based FTC effectiveness (before and after the control gain adjustment using LQR), so that the FTC improvement of the LQR adjustment can be presented.

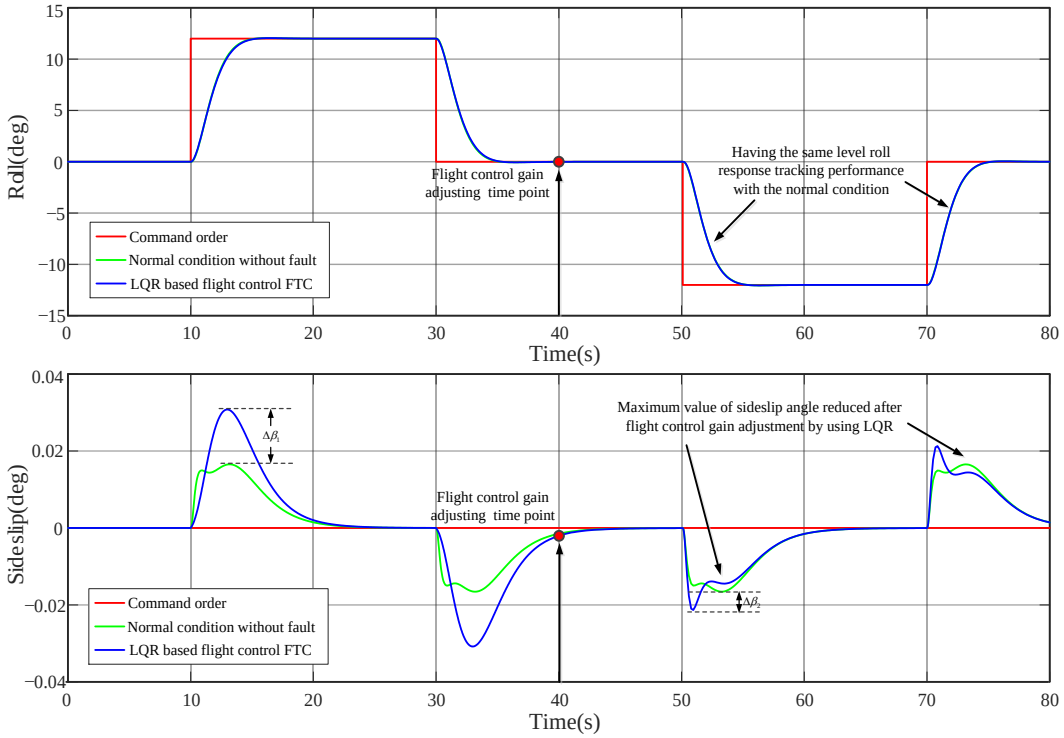


Figure 10. Comparison of the flight control level FTC effectiveness based on the LQR adjustment.

As shown in Figure 10, by using the LQR controller-based flight control level FTC strategy, all the NT-DRASs do not switch channels. Instead, the control gains at the flight control level are globally adjusted through the LQR controller, essentially compensating for the required actions of the failed or degraded control surfaces by increasing the gains of other effective control surfaces. The switching occurs in the 40th second. Before switching, it can be observed from the response of the NSV model's roll and sideslip angles that the response of the roll angle is basically the same as that of the normal condition. However, due to partial NT-DRAS channel failures, the sideslip angle fluctuates to about twice the normal level. After the gain adjustment through the LQR controller, the response of simulated sideslip angle in the subsequent 40s shows that although the sideslip angle does not completely overlap with the situation before the LQR controller gain adjustment, the amplitude of fluctuation is essentially suppressed to the level of the normal condition ($\Delta\beta_2 \ll \Delta\beta_1$).

4.3.4. Summary of the Different Level-Based FTC Effectiveness Analysis

As can be seen from the simulation effect of the two-level switching strategies in Figures 9 and 10, the NT-DRAS channel switching and the LQR gain adjustment are able to realize the desired FTC performance for the NSV model, whereby the NT-DRAS channel switching strategy at the actuation system level has the best FTC effect because it adopts a new channel to completely replace the faulty channel. The cost is that the backup margin resources are enabled. The LQR gain adjustment at the flight control level can basically

achieve the same performance as that of the normal operating condition, but at the cost of a high level of controller gain changes, and the large gain may bring problems of energy consumption and the adaptability of the full operating conditions. In order to form a hierarchical FTC strategy, the solution given in this paper is based on the principle of safety combined with performance. During the first FTC process, the LQR global gain adjustment at the flight control level is carried out in the event of NT-DRAS channel failure or performance degradation. When this gain adjustment cannot meet the NSV safety and performance requirements, the faulty NT-DRAS current working channel is switched. This FTC measure is carried out at the expense of the residual resources. Finally, if all the NT-DRASs of the actuation system level have already carried out channel switching and no residual resources are left, then the LQR secondary global gain adjustment at the flight control level is used to perform FTC again, thus forming a hierarchical multi-level FTC strategy to cope with ever-increasing faults.

4.4. Verification of the Designed Observer Convergence

4.4.1. Solved Observer Gain Matrix

To generate the feedback control law when sensor system faults occur, the concomitant observer states are used to replace the sensors failures caused unknown NSV states. The concomitant observer gain can be solved by using the algorithm in Theorem 1. To improve the convergence efficiency, the adjustment coefficient was chosen as $\rho_{\text{ob}} = 2.878\text{e} - 07$. Finally, the used observer gain may be determined as follows:

$$\boldsymbol{L}_{\text{actual}} = \begin{bmatrix} 1.9882 & 0.0283 & -0.9176 & -0.0456 \\ 0.0282 & 0.3417 & 0.0102 & 0.5714 \\ -0.9176 & 0.0102 & 0.4269 & 0.0602 \\ -0.0455 & 0.5714 & 0.0602 & 0.9612 \end{bmatrix} \tag{25}$$

4.4.2. Observer Convergence Simulation Verification

In order to guarantee that the concomitant observer can achieve convergence to the real NSV model, so that the concomitant observer states can be used to perform the FTC law, different command signals, including step one as well as sine one, are used to simulate the observer convergence. Figures 11 and 12 show the error curves between the observer and the actual NSV model when given step and sine signals respectively, so that the observer convergence can be verified.

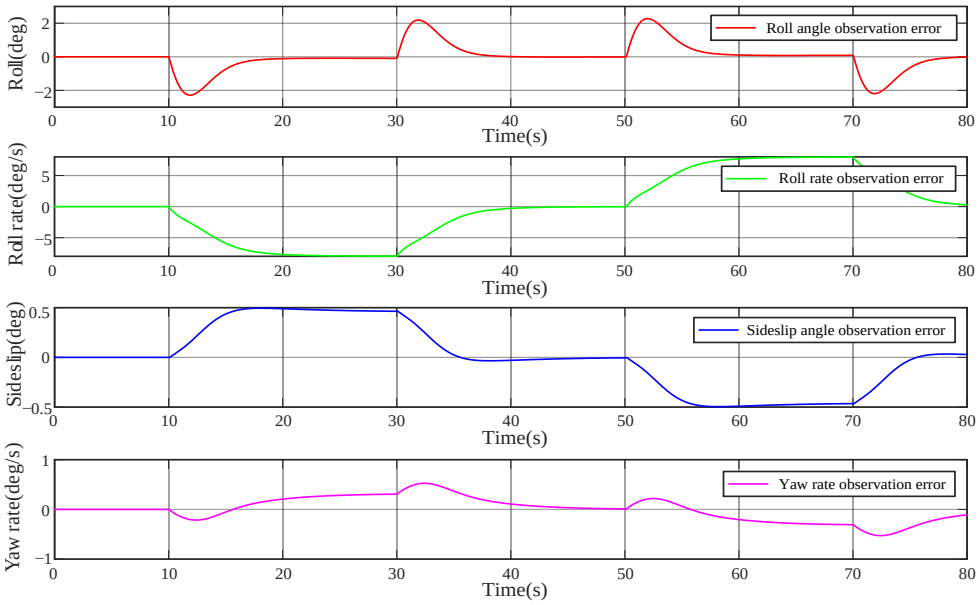


Figure 11. Observer state convergence errors when given a step signal.

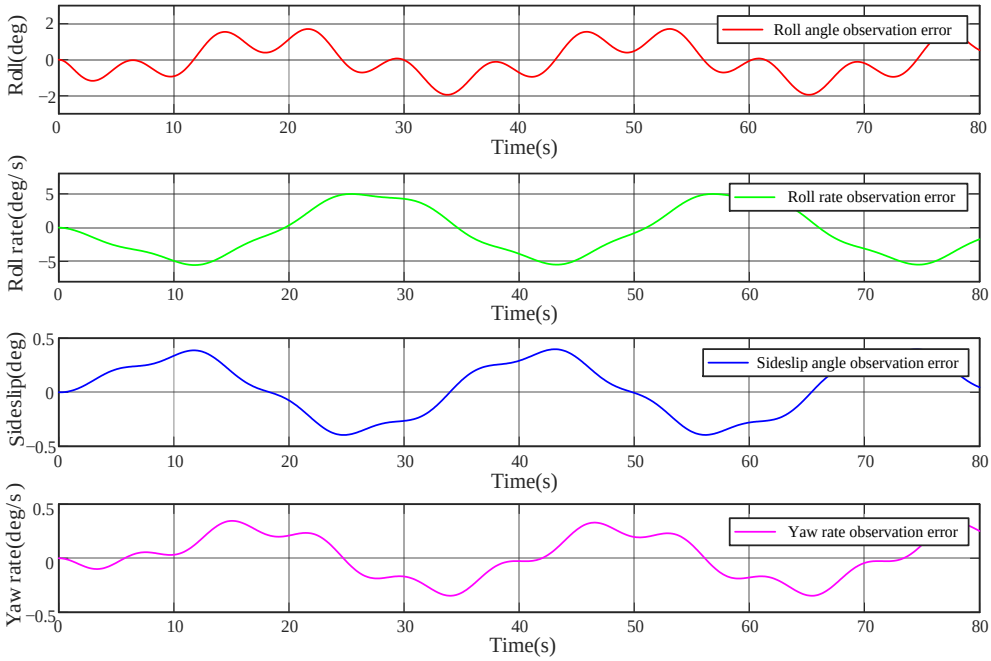


Figure 12. Observer state convergence errors when given a sine signal.

In Figures 11 and 12, the given roll angle reference signal has a maximum magnitude value of 12°. The maximum observation error of the roll angle is about 2°, whose amplitude is small and can be converged to 0 in about 5s. The maximum amplitude of the error curve of the roll angle rate is about 7°/s, which can be converged to the actual system as well. Though this rate is not the final output of the NSV model, the error amplitude and convergence results also meet the observer design requirements. The estimated error of the sideslip angle is about 0.5° or less and can eventually converge. The estimated error amplitude of the yaw angular velocity is within 0.5°/s, which also meets the convergence requirement. These simulation results can be used to verify the algorithm in Theorem 1.

4.5. Response Comparisons of Sensor and NT-DRAS Fault Conditions

4.5.1. FTC Strategy Illustrations

To compare the effectiveness of the FTC, the following different strategies are given:

Strategy-1(S-1). A baseline controller-based control strategy (the NSV state feedback-based control law without observer design).
Strategy-2(S-2). A fixed structure observer-based LQR-FTC strategy.
Strategy-3(S-3). A concomitant observer-based LQR-FTC strategy.

4.5.2. Response Comparison Using S-1 and S-3 under the Changing Fault Conditions in Case 2 and Case 3

Figure 13 shows a comparison of the tracking performance using S-1 and S-3. The concomitant observer dynamic response and the real system responses using the baseline control law and the FTC law are presented in this figure.

As shown in Figure 13, even though some current NT-DRAS working channels are suffering performance degradations or failures, and in addition to the sensor faults, the NSV roll response command can still be tracked well using S-3. Compared with the concomitant observer response, there is only a little response lag. However, by using S-1, the roll state yields no response. Meanwhile, the sideslip response can retain a small oscillation value by using S-3 while the sideslip response diverges by using S-1. The comparison shows that S-3 is still effective under simultaneous NT-DRAS and sensor fault conditions. The quantization statistics in Table 2 also indicate the same conclusion.

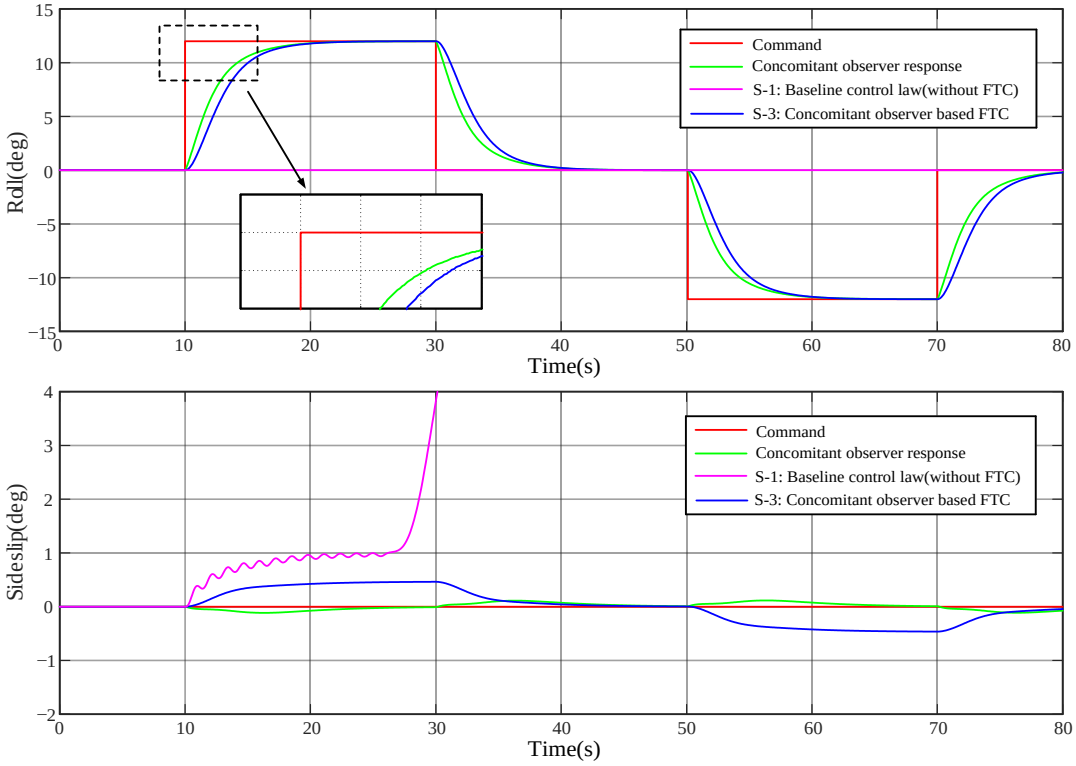


Figure 13. Comparison of the tracking performance using S-1 and S-3.

Table 2. Quantization statistics results for response comparison using S-1 and S-3.

Result Types	Observer Output	By Using S-3	By Using S-1
$e_{\text{perf}-\phi}(t)$	112.27	131.57	unbounded
$e_{\text{perf}-\beta}(t)$	1.80	9.31	unbounded

Only the 2-Norm form $e_{\text{perf}}(t)$ quantization statistics results are used here.

4.5.3. Response Comparison Using S-2 and S-3 under Changing Fault Conditions from Case 1 to Case 4

Hybrid State Generation Mechanism in S-3

Figure 14 shows the hybrid state generation principle when using the concomitant observer-based FTC method (S-3).

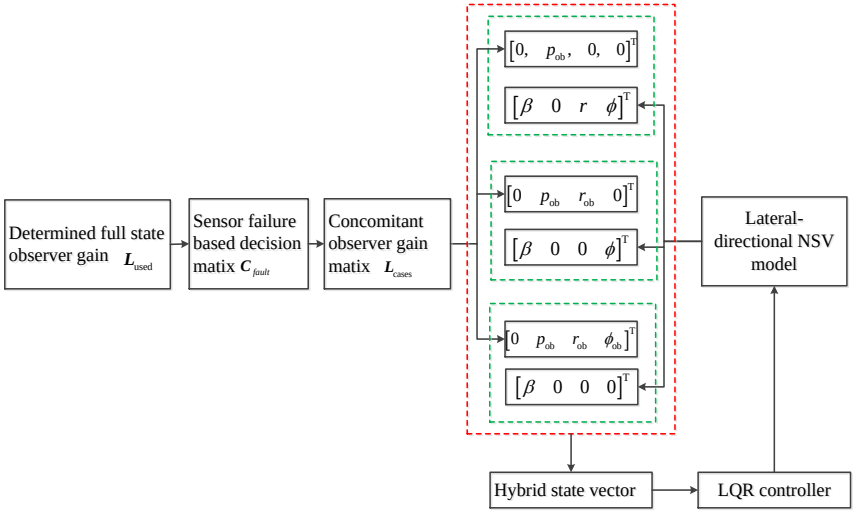


Figure 14. Hybrid states vector by using concomitant observer states in S-3.

As shown in Figure 14, under sensor fault cases 2–4, the hybrid states can be integrated by using the concomitant observer states and the NSV left normal states. By changing the corresponding dimension of the concomitant observer, only if the unknown states due to sensor failures are obtained can the observation errors of the left normal states be avoided.

To verify the advantages of S-3 and compare it with S-2, the fault conditions are assumed to change. In every specific case, the concomitant observer can change its corresponding dimension to obtain the missing unknown states. Composing the concomitant estimated states with the NSV left normal states can result in the concomitant observer-based FTC law, as shown in Equation (26). The missing roll rate is estimated as p_{ob}, while the missing roll and yaw rates are estimated as p_{ob} and r_{ob}, respectively, in Case 2. The missing roll and yaw rates and roll angle are estimated as p_{ob}, r_{ob}, and ϕ_{ob}, respectively, in Case 4. The concomitant observer changes its corresponding dimensions with the failed sensor while the observer gain matrix also changes to fit with the specific cases. However, S-2 always uses the originally determined gain matrix, even under changing conditions.

$$\begin{cases} \boldsymbol{L}^{\mathrm{FTC}}_{\mathrm{case}-2} = \begin{bmatrix} 0.0281 & 0.3416 & 0.0103 & 0.5712 \end{bmatrix} \\ \boldsymbol{x}_{\mathrm{hybrid}} = \begin{bmatrix} \beta & p_{\mathrm{ob}} & r & \phi \end{bmatrix}^{\mathrm{T}} \\ \boldsymbol{L}^{\mathrm{FTC}}_{\mathrm{case}-3} = \begin{bmatrix} 0.0281 & 0.3416 & 0.0103 & 0.5712 \\ -0.9177 & 0.0103 & 0.4268 & 0.0603 \end{bmatrix} \\ \boldsymbol{x}_{\mathrm{hybrid}} = \begin{bmatrix} \beta & p_{\mathrm{ob}} & r_{\mathrm{ob}} & \phi \end{bmatrix}^{\mathrm{T}} \\ \boldsymbol{L}^{\mathrm{FTC}}_{\mathrm{case}-4} = \begin{bmatrix} 0.0281 & 0.3416 & 0.0103 & 0.5712 \\ -0.9177 & 0.0103 & 0.4268 & 0.0603 \\ -0.0456 & 0.5715 & 0.0605 & 0.9613 \end{bmatrix} \\ \boldsymbol{x}_{\mathrm{hybrid}} = \begin{bmatrix} \beta & p_{\mathrm{ob}} & r_{\mathrm{ob}} & \phi_{\mathrm{ob}} \end{bmatrix}^{\mathrm{T}} \end{cases} \tag{26}$$

The control gain under the normal condition is solved as $\boldsymbol{K}^{\mathrm{base}}_{\mathrm{Case}-1}$ in Equation (23), while the FTC gain under Case 2 is solved as $\boldsymbol{K}^{\mathrm{FTC}}_{\mathrm{Case}-2}$ in Equation (24). The FTC gain under Case 3 is solved as $\boldsymbol{K}^{\mathrm{FTC}}_{\mathrm{Case}-3}$ in Equation (27). Since in Case 4, some current NT-DRAS channel performance indices are too low, the solved FTC gain based on these indices cannot achieve the desired control performance. Therefore, the LQR-based flight control gain adjustment is not used for Case 4; rather, the NT-DRAS channel switching strategy is used so that NT-DRASs performance health status matrix $\boldsymbol{H}^{\mathrm{NT-DRAS}}_{\mathrm{Case}-4} = diag\{0 \quad 0.11 \quad 0.23 \quad 0.17 \quad 0\}$ can be updated to a new one as $\boldsymbol{H}^{\mathrm{NT-DRAS}}_{\mathrm{Case}-4(\mathrm{FTC})} = \boldsymbol{H}^{\mathrm{NT-DRAS}}_{\mathrm{Case}-1} = diag\{1 \quad 1 \quad 1 \quad 1 \quad 1\}$. Therefore, the control gain under Case 4 can be chosen as $\boldsymbol{K}^{\mathrm{FTC}}_{\mathrm{Case}-4} = \boldsymbol{K}^{\mathrm{base}}_{\mathrm{Case}-1}$.

$$\boldsymbol{K}^{\mathrm{FTC}}_{\mathrm{Case}-3} = \begin{bmatrix} 0 & 0 & 0 & 0 & 0 & 0 \\ -10.1072 & 19.9171 & 5.1036 & 32.7921 & -18.0514 & 1.8605 \\ -8.3571 & 28.6974 & 6.3506 & 47.1967 & -25.9299 & 0.3317 \\ 82.1166 & 4.9610 & -46.2800 & 3.7420 & -1.3364 & -31.5663 \\ 0 & 0 & 0 & 0 & 0 & 0 \end{bmatrix} \tag{27}$$

Response comparison using S-2 and S-3 when given specific step signal.

Figure 15 shows a tracking response performance comparison result using S-2 and S-3 when given a step signal. The dynamic performance improvement when using concomitant observer-based FTC is illustrated in this figure.

It can be seen from Figure 15 that when a step signal is given to the NSV model, both S-2 and S-3 can make the NSV respond to the given command effectively, although the response performances are different. The rising time of the NSV roll response is about 5 s using S-3, while it is about 10 s using S-2. The maximum oscillation value of the sideslip angle is 0.05° using S-3, while it is about 0.5° using S-2. The dynamic response results show that S-3 can achieve better FTC performance not only in terms of a quick response, but also in terms of stability and flight control quality. The quantization statistic results in Table 3 also yield the same conclusion.

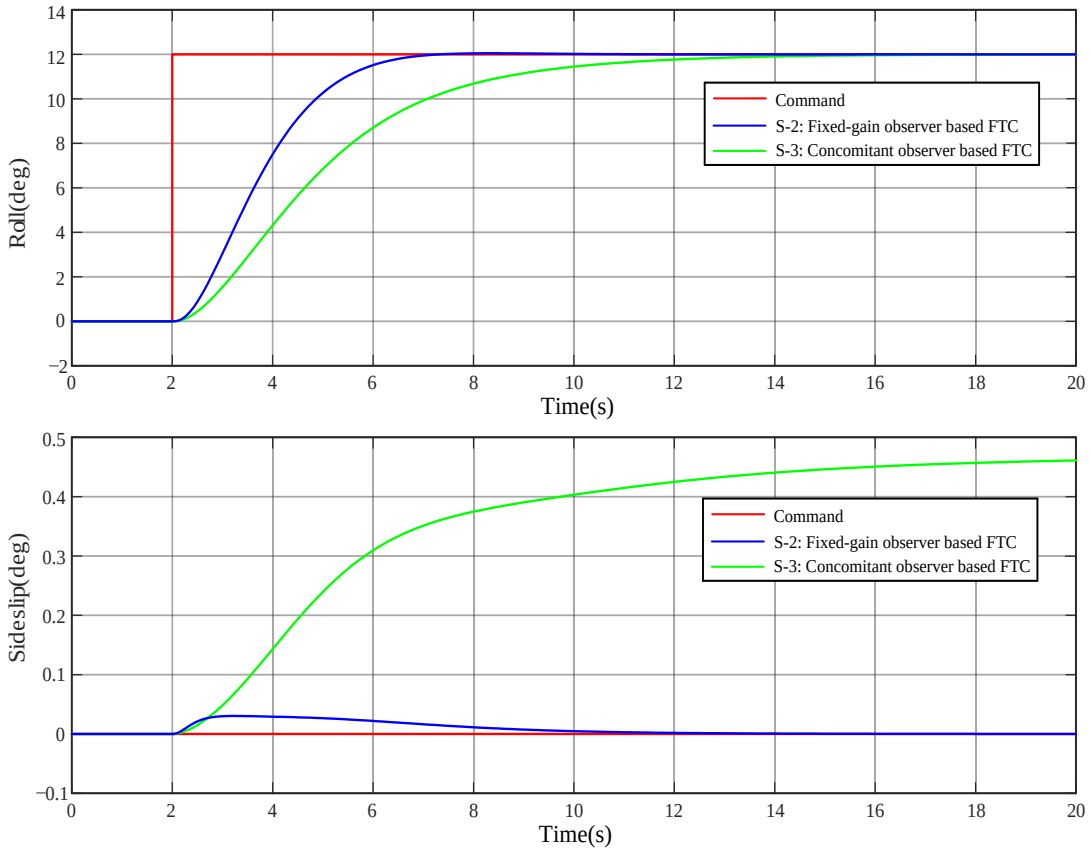


Figure 15. Tracking response performance comparison using S-2 and S-3 when given a step signal.

Table 3. Quantization statistic results for a response comparison using S-2 and S-3.

Result Types	By Using S-2	By Using S-3
$e_{\text{perf}-\phi}(t)$	63.89	53.07
$e_{\text{perf}-\beta}(t)$	5.55	0.20

Only the 2-Norm form $e_{\text{perf}}(t)$ quantization statistics results are used here.

Response comparison using S-2 and S-3 under changing fault conditions from Case 1 to Case 4

For the changing and worsening cases of the NSV model, the fault changing times are set as 13 s (Case 1 to Case 2), 43 s (Case 2 to Case 3), and 73 s (Case 3 to Case 4). It is assumed that the FDD mechanism can detect the fault information immediately and the FTC measures can also be performed quickly.

Figure 16 shows a tracking response performance comparison when the NSV maintains a constant roll angle using S-2 and S-3. The tracking performance improvement when using concomitant observer-based FTC is illustrated in this figure.

As shown in Figure 16, the fault change occurs when the NSV maintains a constant roll command angle of 12°. The roll angle fluctuations are small by using both S-2 and S-3 (see Table 4: roll response performance). However, the NSV can achieve better stability by using S-3. It can be seen from the fault changing process from Case1 to Case 2 that S-3-based FTC can assure a smaller sideslip angle and better roll action performance. It can be seen from the fault changing process from Case 2 to Case 3 that the NSV can have a smaller sideslip angle by using S-3 compared with S-2 (a longer time is necessary for the sideslip angle converges to 0°). When the fault condition changes to Case 4, the fault NT-DRAS channels have to be switched to update the health indices. Though the roll angle fluctuation is bigger when using S-3, it can result in very small sideslip angle, i.e., within 0.05°, while it is more than 0.12° with S-2. It can be concluded that the concomitant observer-based S-3

FTC strategy can result in better tracking performance because of the hybrid state-based FTC control law. It can be seen from Table 4 that the sideslip response fluctuation can be reduced about 50% by using S-3.

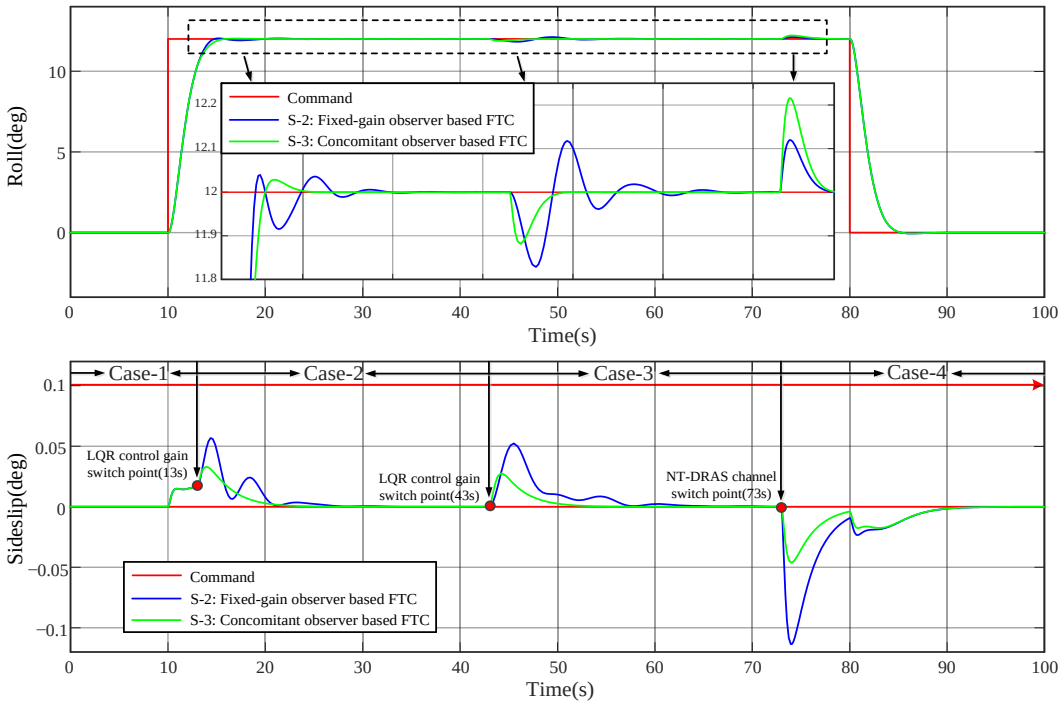


Figure 16. Tracking response performance comparison when the NSV maintains a constant roll angle.

Table 4. Quantization statistic results for our response comparison using S-2 and S-3 under changing fault conditions (fault condition changes during a steady process).

Strategy	Roll Response Performance			Sideslip Response Performance		
	$e_{\mathbf{perf}-\phi}(t)$	$\bar{e}_{\mathbf{perf}-\phi}(t)$	$e^{\mathbf{max}}_{\mathbf{perf}-\phi}(t)$	$e_{\mathbf{perf}-\beta}(t)$	$\bar{e}_{\mathbf{perf}-\beta}(t)$	$e^{\mathbf{max}}_{\mathbf{perf}-\beta}(t)$
S-2	60.4618	0.008991	12	0.47768	0.0001115	0.113
S-3	60.4597	0.008991	12	0.23987	0.0000621	0.045

Fault condition changes when the roll command maintains a constant value.

Figure 17 shows a tracking response performance comparison when the NSV has a dynamic changing roll action using S-2 and S-3. During this dynamic process, when the faults occur and the fault cases become worse, the FTC advantage of S-3 is illustrated in this figure.

As shown in Figure 17, the fault change occurs when the NSV has a dynamic changing roll action ($0^\circ \rightarrow 12^\circ \rightarrow -12^\circ \rightarrow 0^\circ$). From the dynamic process from Case 1 to Case 2, both S-2- and S-3-based FTC strategies can maintain the desired NSV tracking performance, while S-3-based FTC can achieve a smaller sideslip angle. The dynamic process from Case 2 to Case 3 shows that the NSV can achieve a quicker roll step signal response with no fluctuations by using S-3 compared with S-2 (an overshoot angle of more than 5° occurs with fluctuations). Meanwhile, the sideslip angle is within a limited amplitude (0.1°) when using S-3, while it fluctuates during within an interval of -0.6° to 0.4° when using S-2. When the fault condition changes to Case 4, all the faulty NT-DRAS channels are updated. The roll action is still quicker with no overshoot when using S-3 compared with S-2. Additionally, the maximum sideslip angle is within 0.1° when using S-3, while it is bigger than 0.4° when using S-2. Table 5 shows that the roll response tracking error can be reduced by about 6.85% by using S-3. The sideslip response fluctuation can be reduced by about 81.98% by using S-3. It can concluded that the concomitant observer-based S-3

FTC strategy is more suitable for the changing fault conditions compared with the fixed structure-based S-2 FTC strategy.

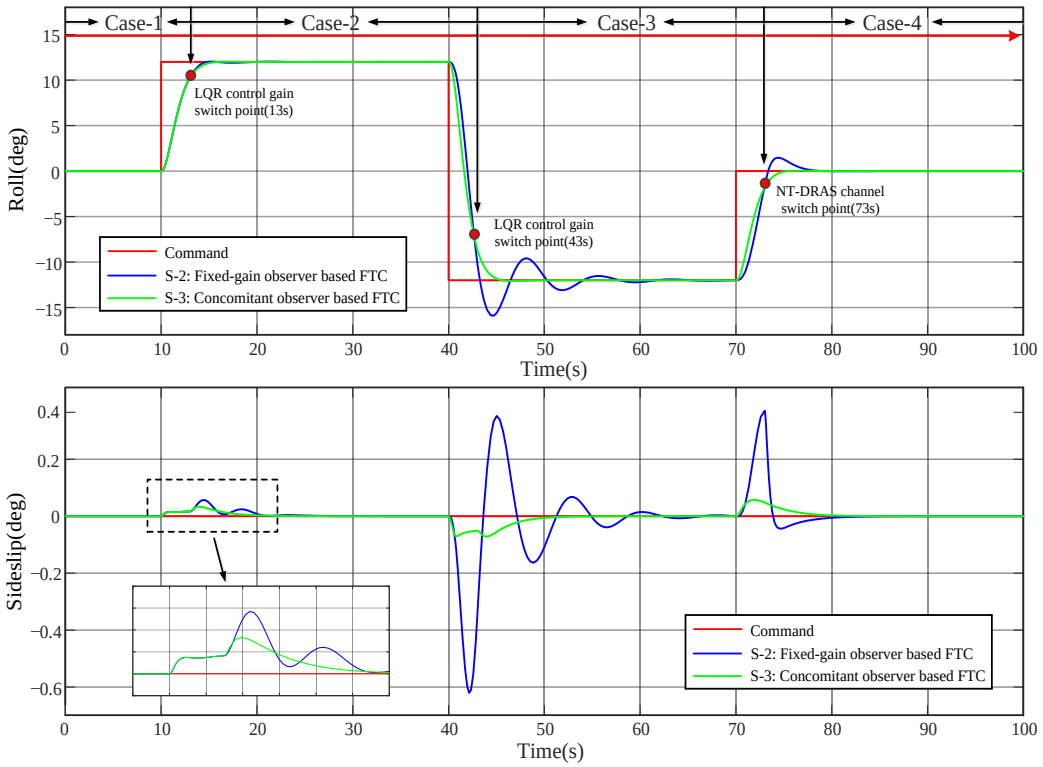


Figure 17. Tracking response performance comparison when the NSV has a dynamic changing roll action.

Table 5. Quantization of the statistic results for a response comparison using S-2 and S-3 under changing fault conditions (fault condition changes during a dynamic process).

Strategy	Roll Response Performance			Sideslip Response Performance		
	$e_{\mathbf{perf}-\phi}(t)$	$\bar{e}_{\mathbf{perf}-\phi}(t)$	$e^{\max}_{\mathbf{perf}-\phi}(t)$	$e_{\mathbf{perf}-\beta}(t)$	$\bar{e}_{\mathbf{perf}-\beta}(t)$	$e^{\max}_{\mathbf{perf}-\beta}(t)$
S-2	121.3271	0.020723	24	2.5843	0.0004727	0.62
S-3	113.0101	0.018318	24	0.4657	0.0001072	0.07

Fault condition changes when the roll command also changes.

5. Discussion

The paper proposes a concomitant observer-based multi-level FTC algorithm for NSVs with NT-DRASs under complex changing fault conditions. Compared with previous studies, the following points should be stressed:

(1) Previous works have usually presented simplified actuation systems in flight control model, e.g., [11–14], while in this paper, both the EHA and EMA channels of the NT-DRAS were modeled in the NSV input link. Additionally, previous works usually focused on certain specific fault conditions and used a fixed structure observer to determine the causes of sensor fault states, e.g., [19–22,24], while in this paper, a new conceptual concomitant observer was used for the complex changing fault conditions. In one word, the NT-DRAS and a concomitant observer are integrated to form a multi-level FTC mechanism, which was the motivation of our research;

(2) The discussed NSV with NT-DRASs is a kind of highly intelligent and reliable aircraft. The proposed multi-level FTC strategy can utilize the NT-DRAS hardware resources to perform intelligent flight control algorithms at the NT-DRAS level as well as at the flight control level, thereby giving the NSV strong viability under most fault conditions;

(3) There were four assumptions (Assumption 1–4) in this paper. The proposed FTC strategy needs to be performed on at least one set of actuation channels for the corresponding main safety control surfaces to be able to work. Under certain extreme fault conditions, such as structural damaged, other FTC strategies need to be developed; this will serve as the basis for the future work. Additionally, the proposed multi-level algorithm has to be performed using LQR control gain adjustments at the flight control level and NT-DRAS channel switching at the actuation system level. The switching can cause transient performance changes in the NSV; this aspect needs to be optimized.

6. Conclusions

The paper proposes an intelligent and highly reliable, multi-level FTC strategy for NSVs with NT-DRASs. The FTC resources in the actuation level increased by 200% due to the integrated EHA and EMA channels in the NT-DRAS, and the FTC circle can be performed at both the flight control level and NT-DRAS level. For actuation system faults, as two different levels of FTC measures, the flight control gain adjustment strategy can recover the flight quality to a certain level without using the FTC resources, while the NT-DRAS channel switching measure can recover 100% flight quality since the current fault channel is switched to a healthy backup one. Further considering the sensor faults, compared with the fixed structure observer-based LQR-FTC, the concomitant observer-based one offers obvious flight quality improvements, especially under changing fault cases, e.g., as shown in Figure 17, where even though the tracking error was only reduced by less than 7%, the response fluctuation could be reduced more than 80%. To perform the proposed FTC measures, the health status matrices of the NT-DRASs and sensors were assumed to be known and could be updated in real-time. Therefore, determining how to integrate and optimize the criteria of the FDD and FTC schemes so that the NSVs can achieve stress responsiveness to comprehensive faults can be listed as the most important aspect of future work in this field.

Author Contributions: Conceptualization, M.W. and J.W.; methodology, J.W.; validation, J.W.; formal analysis, J.H.; investigation, M.W.; resources, M.W.; data curation, J.W.; writing—original draft preparation, M.W.; writing—review and editing, M.W.; visualization, J.W.; supervision, J.H.; project administration, J.W.; funding acquisition, J.W. All authors have read and agreed to the published version of the manuscript.

Funding: This work was supported by the National Natural Science Foundation of China (Grant No. 52105049 and 52175038).

Data Availability Statement: Data are contained within the article.

Conflicts of Interest: The authors declare no conflict of interest.

Appendix A

Proof of Theorem 1. For the error system form in Equation (17), a disturbance attenuation level constant is given as γ_{ob}. Then a sufficient condition of the concomitant observer convergence can be restated as

$$(\boldsymbol{A}_{\mathrm{normal}} + \boldsymbol{B}_{fault}\boldsymbol{K}_{\boldsymbol{x}} - \boldsymbol{L}_{\mathrm{ob}}\boldsymbol{C}_{fault})^{\mathrm{T}}\boldsymbol{P}_{\mathrm{ob}} + \boldsymbol{P}_{\mathrm{ob}}(\boldsymbol{A}_{\mathrm{normal}} + \boldsymbol{B}_{fault}\boldsymbol{K}_{\boldsymbol{x}} - \boldsymbol{L}_{\mathrm{ob}}\boldsymbol{C}_{fault}) + \left(\frac{1}{\gamma_{\mathrm{ob}}^2}\right)\boldsymbol{P}_{\mathrm{ob}}\boldsymbol{G}\boldsymbol{G}^{\mathrm{T}}\boldsymbol{P}_{\mathrm{ob}} < \boldsymbol{0} \quad \text{(A1)}$$

By using the Reciprocal Projection Lemma used in [35] and defining $\boldsymbol{\psi}_{\mathrm{ob}} = \left(\frac{1}{\gamma_{\mathrm{ob}}^2}\right)\boldsymbol{P}_{\mathrm{ob}}\boldsymbol{G}\boldsymbol{G}^{\mathrm{T}}\boldsymbol{P}_{\mathrm{ob}}$ and $\boldsymbol{\zeta}_{\mathrm{ob}} = \boldsymbol{P}_{\mathrm{ob}}\left(\boldsymbol{A}_{\mathrm{normal}} + \boldsymbol{B}_{fault}\boldsymbol{K}_{\boldsymbol{x}} - \boldsymbol{L}_{\mathrm{ob}}\boldsymbol{C}_{fault}\right)$, Equation (A1) can be derived into the form in Equation (A2):

$$\begin{bmatrix} \left(\frac{1}{\gamma_{\mathrm{ob}}^2}\right)\boldsymbol{P}_{\mathrm{ob}}\boldsymbol{G}\boldsymbol{G}^{\mathrm{T}}\boldsymbol{P}_{\mathrm{ob}} + \boldsymbol{P}_{\mathrm{ob}} - \left(\boldsymbol{S}_{\mathrm{ob}} + \boldsymbol{S}_{\mathrm{ob}}^{\mathrm{T}}\right) & \boldsymbol{S}_{\mathrm{ob}}^{\mathrm{T}} + \left(\boldsymbol{A}_{\mathrm{normal}} + \boldsymbol{B}_{fault}\boldsymbol{K}_{\boldsymbol{x}} - \boldsymbol{L}_{\mathrm{ob}}\boldsymbol{C}_{fault}\right)^{\mathrm{T}}\boldsymbol{P}_{\mathrm{ob}} \\ \boldsymbol{S}_{\mathrm{ob}} + \boldsymbol{P}_{\mathrm{ob}}\left(\boldsymbol{A}_{\mathrm{normal}} + \boldsymbol{B}_{fault}\boldsymbol{K}_{\boldsymbol{x}} - \boldsymbol{L}_{\mathrm{ob}}\boldsymbol{C}_{fault}\right) & -\boldsymbol{P}_{\mathrm{ob}} \end{bmatrix} < \boldsymbol{0} \tag{A2}$$

By a congruence transformation matrix $\begin{bmatrix} \boldsymbol{V}_{\mathrm{ob}} & \boldsymbol{0} \\ \boldsymbol{0} & \boldsymbol{X}_{\mathrm{ob}} \end{bmatrix}$ with $\boldsymbol{V}_{\mathrm{ob}} = \boldsymbol{S}_{\mathrm{ob}}^{-1}$ and $\boldsymbol{X}_{\mathrm{ob}} = \boldsymbol{P}_{\mathrm{ob}}^{-1}$, the following inequality can be obtained:

$$\begin{bmatrix} \left(\frac{1}{\gamma_{\mathrm{ob}}^2}\right)\boldsymbol{V}_{\mathrm{ob}}^{-1}\boldsymbol{P}_{\mathrm{ob}}\boldsymbol{G}\boldsymbol{G}^{\mathrm{T}}\boldsymbol{P}_{\mathrm{ob}}\boldsymbol{V}_{\mathrm{ob}} + \boldsymbol{V}_{\mathrm{ob}}^{-1}\boldsymbol{P}_{\mathrm{ob}}\boldsymbol{V}_{\mathrm{ob}} - \left(\boldsymbol{V}_{\mathrm{ob}} + \boldsymbol{V}_{\mathrm{ob}}^{\mathrm{T}}\right) & \boldsymbol{X}_{\mathrm{ob}}^{\mathrm{T}} + \boldsymbol{V}_{\mathrm{ob}}^{\mathrm{T}}\left(\boldsymbol{A}_{\mathrm{normal}} + \boldsymbol{B}_{fault}\boldsymbol{K}_{\boldsymbol{x}} - \boldsymbol{L}_{\mathrm{ob}}\boldsymbol{C}_{fault}\right)^{\mathrm{T}} \\ \boldsymbol{X}_{\mathrm{ob}} + \left(\boldsymbol{A}_{\mathrm{normal}} + \boldsymbol{B}_{fault}\boldsymbol{K}_{\boldsymbol{x}} - \boldsymbol{L}_{\mathrm{ob}}\boldsymbol{C}_{fault}\right)\boldsymbol{V}_{\mathrm{ob}} & -\boldsymbol{X}_{\mathrm{ob}} \end{bmatrix} < \boldsymbol{0} \tag{A3}$$

By using the Schur Complement Lemma [36], Equation (A3) can be transformed to following form:

$$\begin{bmatrix} -\left(\boldsymbol{V}_{\mathrm{ob}} + \boldsymbol{V}_{\mathrm{ob}}^{\mathrm{T}}\right) & \boldsymbol{X}_{\mathrm{ob}} + \boldsymbol{V}_{\mathrm{ob}}^{\mathrm{T}}\boldsymbol{A}^{\mathrm{T}} + \boldsymbol{V}_{\mathrm{ob}}^{\mathrm{T}}\left(\boldsymbol{B}_{fault}\boldsymbol{K}_{\boldsymbol{x}}\right)^{\mathrm{T}} - \left(\boldsymbol{L}_{\mathrm{ob}}\boldsymbol{C}_{fault}\boldsymbol{V}_{\mathrm{ob}}\right)^{\mathrm{T}} & \boldsymbol{V}_{\mathrm{ob}}^{\mathrm{T}} & \boldsymbol{V}_{\mathrm{ob}}^{\mathrm{T}}\boldsymbol{P}_{\mathrm{ob}}\boldsymbol{G} \\ * & -\boldsymbol{X}_{\mathrm{ob}} & 0 & 0 \\ * & * & -\boldsymbol{X}_{\mathrm{ob}} & 0 \\ * & * & * & -\gamma_{\mathrm{ob}}^2\boldsymbol{I} \end{bmatrix} < \boldsymbol{0} \tag{A4}$$

Since Equation (A4) is not a linear matrix, it needs to be linearized. By defining $\boldsymbol{N}_{\mathrm{ob}} = \boldsymbol{L}_{\mathrm{ob}}\boldsymbol{C}_{fault}\boldsymbol{V}_{\mathrm{ob}}$ and $\boldsymbol{M}_{\mathrm{ob}} = \boldsymbol{P}_{\mathrm{ob}}\boldsymbol{V}_{\mathrm{ob}}$, the LMI form can be derived as follows:

$$\begin{bmatrix} -\left(\boldsymbol{V}_{\mathrm{ob}} + \boldsymbol{V}_{\mathrm{ob}}^{\mathrm{T}}\right) & \boldsymbol{X}_{\mathrm{ob}} + \boldsymbol{V}_{\mathrm{ob}}^{\mathrm{T}}\boldsymbol{A}_{\mathrm{normal}}^{\mathrm{T}} + \boldsymbol{V}_{\mathrm{ob}}^{\mathrm{T}}\left(\boldsymbol{B}_{fault}\boldsymbol{K}_{\boldsymbol{x}}\right)^{\mathrm{T}} - \left(\boldsymbol{N}_{\mathrm{ob}}\right)^{\mathrm{T}} & \boldsymbol{V}_{\mathrm{ob}}^{\mathrm{T}} & \boldsymbol{M}_{\mathrm{ob}}^{\mathrm{T}}\boldsymbol{G} \\ * & -\boldsymbol{X}_{\mathrm{ob}} & 0 & 0 \\ * & * & -\boldsymbol{X}_{\mathrm{ob}} & 0 \\ * & * & * & -\gamma_{\mathrm{ob}}^2\boldsymbol{I} \end{bmatrix} < \boldsymbol{0} \tag{A5}$$

The concomitant observer gain in full state observer form can be solved as $\boldsymbol{L}_{\mathrm{ob}} = \boldsymbol{N}_{\mathrm{ob}}\boldsymbol{V}_{\mathrm{ob}}^{-1}$ by using the LMI technique first, and then the concomitant observer gain for the changing fault cases can furthermore be determined as $\boldsymbol{L}_{fault} = \boldsymbol{N}_{\mathrm{ob}}\boldsymbol{V}_{\mathrm{ob}}^{-1}\boldsymbol{C}_{fault}^{-1}$.

End the proof. □

Appendix B

Proof of Theorem 2.

$$\begin{aligned} J_{\mathrm{LQ}} &= \int_0^t \boldsymbol{x}_{\mathrm{aug}}^{\mathrm{T}}(\tau)\left(\boldsymbol{Q} + \boldsymbol{K}_{flight}^{\mathrm{T}}\boldsymbol{R}\boldsymbol{K}_{flight}\right)\boldsymbol{x}_{\mathrm{aug}}(\tau)d\tau \\ &< -\int_0^t \boldsymbol{x}_{\mathrm{aug}}^{\mathrm{T}}(\tau)\left[\left(\boldsymbol{A}_{\mathrm{aug}} + \boldsymbol{B}_{\mathrm{aug}}\boldsymbol{K}_{flight}\right)^{\mathrm{T}}\boldsymbol{P}_{\mathrm{c}} + \boldsymbol{P}_{\mathrm{c}}\left(\boldsymbol{A}_{\mathrm{aug}} + \boldsymbol{B}_{\mathrm{aug}}\boldsymbol{K}_{flight}\right) + \left(\frac{1}{\gamma_{\mathrm{c}}^2}\right)\boldsymbol{P}_{\mathrm{c}}\boldsymbol{G}_{\mathrm{aug}}\boldsymbol{G}_{\mathrm{aug}}^{\mathrm{T}}\boldsymbol{P}_{\mathrm{c}}\right]\boldsymbol{x}_{\mathrm{aug}}(\tau)d\tau \\ &= -\int_0^t \left[\left(\dot{\boldsymbol{x}}_{\mathrm{aug}}(\tau) - \boldsymbol{G}_{\mathrm{aug}}\boldsymbol{w}_{\mathrm{aug}}(\tau)\right)^{\mathrm{T}}\boldsymbol{P}_{\mathrm{c}}\boldsymbol{x}_{\mathrm{aug}}(\tau) + \boldsymbol{x}_{\mathrm{aug}}^{\mathrm{T}}(\tau)\boldsymbol{P}_{\mathrm{c}}\left(\dot{\boldsymbol{x}}_{\mathrm{aug}}(\tau) - \boldsymbol{G}_{\mathrm{aug}}\boldsymbol{w}_{\mathrm{aug}}(\tau)\right) + \boldsymbol{x}_{\mathrm{aug}}^{\mathrm{T}}(\tau)\left(\frac{1}{\gamma_{\mathrm{c}}^2}\right)\boldsymbol{P}_{\mathrm{c}}\boldsymbol{G}_{\mathrm{aug}}\boldsymbol{G}_{\mathrm{aug}}^{\mathrm{T}}\boldsymbol{P}_{\mathrm{c}}\boldsymbol{x}_{\mathrm{aug}}(\tau)\right]d\tau \\ &\leq -\int_0^t \boldsymbol{d}\left(\boldsymbol{x}_{\mathrm{aug}}^{\mathrm{T}}(\tau)\boldsymbol{P}_{\mathrm{c}}\boldsymbol{x}_{\mathrm{aug}}(\tau)\right) + \gamma_{\mathrm{c}}^2\int_0^t \boldsymbol{w}_{\mathrm{aug}}^{\mathrm{T}}(\tau)\boldsymbol{w}_{\mathrm{aug}}(\tau)d\tau \\ &= \boldsymbol{x}_{\mathrm{aug}}^{\mathrm{T}}(0)\boldsymbol{P}_{\mathrm{c}}\boldsymbol{x}_{\mathrm{aug}}(0) + \gamma_{\mathrm{c}}^2\int_0^t \boldsymbol{w}_{\mathrm{aug}}^{\mathrm{T}}(\tau)\boldsymbol{w}_{\mathrm{aug}}(\tau)d\tau \end{aligned} \tag{A6}$$

End the proof. □

Appendix C

Proof of Statement 1. For the error observation dynamic system form in Equation (17), it can derive the following equation:

$$\boldsymbol{x}(t) = \tilde{\boldsymbol{x}}(t) + \tilde{\boldsymbol{e}}_{\mathrm{ob}}(t) \tag{A7}$$

By using Theorem 1, since the solved observer gain can guarantee the convergence, therefore, the dynamic system form in Equation (17) is stable, that is

$$\dot{\tilde{\boldsymbol{e}}}_{\mathrm{ob}}(t) = \left(\boldsymbol{A}_{\mathrm{normal}} - \boldsymbol{L}_{\mathrm{ob}}\boldsymbol{C}_{fault}\right)\tilde{\boldsymbol{e}}_{\mathrm{ob}}(t) + \boldsymbol{G}\boldsymbol{\omega}(t) \to 0 \tag{A8}$$

That means $\tilde{\boldsymbol{x}}(t) \to \boldsymbol{x}(t)$. As long as the concomitant observer runs with the real NSV model from the beginning, after the convergence process within a short time, all the substates can also converge to the NSV real states.

By using Theorem 2, it can be seen that each solved LQR control gain can stabilize the NSV model and maintain desired performance in Equation (20). For the control gain switching time, defining $f(t) = \boldsymbol{K}_{\mathrm{now}}(t) = \boldsymbol{K}_{\mathrm{now}}(t_0) + (\boldsymbol{K}_{\mathrm{former}}(t_0) - \boldsymbol{K}_{\mathrm{now}}(t_0))e^{-\tau(t-t_0)}$, then the derivative form can be obtained as following:

$$\begin{aligned} f'(t) &= \tfrac{d\boldsymbol{K}_{\mathrm{now}}(t)}{dt} \\ &= (\boldsymbol{K}_{\mathrm{former}}(t_0) - \boldsymbol{K}_{\mathrm{now}}(t_0))(-\tau)e^{-\tau(t-t_0)} \end{aligned} \tag{A9}$$

Since the fault conditions always become more severe with time, and the LQR control gains need to increase to guarantee the NSV input in the flight control level. Therefore, the control gain norm can satisfy the following inequality:

$$\|\boldsymbol{K}_{\mathrm{former}}(t_0)\| < \|\boldsymbol{K}_{\mathrm{now}}(t_0)\| \to \boldsymbol{K}_{\mathrm{former}}(t_0) - \boldsymbol{K}_{\mathrm{now}}(t_0) < 0 \tag{A10}$$

Since $\tau > 0$, therefore $f'(t) = \frac{d\boldsymbol{K}_{\mathrm{now}}(t)}{dt} > 0$, that means $f(t) = \boldsymbol{K}_{\mathrm{now}}(t)$ can be reguarded as monotonic increasing function in the interval $[t_0, \quad t)$. Therefore, the control gain extremum can be obtained as

$$\begin{cases} \min\boldsymbol{K}(t) = \lim\limits_{t\to t_0}\boldsymbol{K}_{\mathrm{now}}(t) = \boldsymbol{K}_{\mathrm{now}}(t_0) + (\boldsymbol{K}_{\mathrm{former}}(t_0) - \boldsymbol{K}_{\mathrm{now}}(t_0))\left(\lim\limits_{t\to t_0}e^{-\tau(t-t_0)}\right) = \boldsymbol{K}_{\mathrm{former}}(t_0) \\ \max\boldsymbol{K}(t) = \lim\limits_{t\to \infty}\boldsymbol{K}_{\mathrm{now}}(t) = \boldsymbol{K}_{\mathrm{now}}(t_0) + (\boldsymbol{K}_{\mathrm{former}}(t_0) - \boldsymbol{K}_{\mathrm{now}}(t_0))\left(\lim\limits_{t\to \infty}e^{-\tau(t-t_0)}\right) = \boldsymbol{K}_{\mathrm{now}}(t_0) \end{cases} \tag{A11}$$

When the NSV fault case changes and the LQR control gain matrix needs to switch, the NSV performance can still satisfy that

$$\begin{aligned} \boldsymbol{J}_{\mathrm{LQ}} &= \int_0^t \boldsymbol{x}_{\mathrm{aug}}^{\mathrm{T}}(\tau)\left(\boldsymbol{Q} + \boldsymbol{K}_{\mathrm{now}}^{\mathrm{T}}(t)\boldsymbol{R}\boldsymbol{K}_{\mathrm{now}}(t)\right)\boldsymbol{x}_{\mathrm{aug}}(\tau)\boldsymbol{d}\tau \\ &\le \int_0^t \boldsymbol{x}_{\mathrm{aug}}^{\mathrm{T}}(\tau)\left(\boldsymbol{Q} + \boldsymbol{K}_{\mathrm{now}}^{\mathrm{T}}(t_0)\boldsymbol{R}\boldsymbol{K}_{\mathrm{now}}(t_0)\right)\boldsymbol{x}_{\mathrm{aug}}(\tau)\boldsymbol{d}\tau \\ &= \boldsymbol{x}_{\mathrm{aug}}^{\mathrm{T}}(0)\boldsymbol{P}_{\mathrm{c}}\boldsymbol{x}_{\mathrm{aug}}(0) + \gamma_{\mathrm{c}}^2\int_0^t \boldsymbol{w}_{\mathrm{aug}}^{\mathrm{T}}(\tau)\boldsymbol{w}_{\mathrm{aug}}(\tau)\boldsymbol{d}\tau \end{aligned} \tag{A12}$$

Equation (A12) means that the proposed concomitant observer-based multi-level FTC strategy can maintain the NSV model stability, even during the fault case changing times. If the NT-DRAS channel switching occurs to update the current NSV health status, another FTC circle would be reset to perform LQR control gain switching again.

End the proof. □

References

1. Xu, Y.; Jiang, B.; Gao, Z.; Zhang, K. Fault tolerant control for near space vehicle: A survey and some new results. *J. Syst. Eng. Electron.* **2011**, *22*, 88–94.
2. Malyuta, D.; Yu, Y.; Elango, P.; Açıkmeşe, B. Advances in trajectory optimization for space vehicle control. *Annu. Rev. Control* **2021**, *52*, 282–315.
3. Shen, Q.; Jiang, B.; Cocquempot, V. Fuzzy logic system-based adaptive fault-tolerant control for near-space vehicle attitude dynamics with actuator faults. *IEEE Trans. Fuzzy Syst.* **2012**, *21*, 289–300.
4. Qi, H.; Fu, Y.; Qi, X.; Lang, Y. Architecture optimization of more electric aircraft actuation system. *Chin. J. Aeronaut.* **2011**, *24*, 506–513.
5. Wang, S.; Cui, X.; Shi, J.; Tomovic, M.M.; Jiao, Z. Modeling of reliability and performance assessment of a dissimilar redundancy actuation system with failure monitoring. *Chin. J. Aeronaut.* **2016**, *29*, 799–813.
6. Yongling, F.; Yao, P. Design and working mode analysis of dissimilar redundant actuator system. *J. Beijing Univ. Aeronaut. Astronaut.* **2012**, *38*, 432–437.
7. Wang, J.; Wang, S.; Wang, X.; Shi, C.; Tomovic, M.M. Active fault-tolerant control for vertical tail damaged aircraft with dissimilar redundant actuation system. *Chin. J. Aeronaut.* **2016**, *29*, 1313–1325.
8. Huang, J.; Wang, J.; Li, W.; Liu, D.; Shi, C.; Zhang, F. Fault Mode Analysis and Convex Optimization-Based Fault-Tolerant Control for New Type Dissimilar Redundant Actuation System of Near Space Vehicle. *Appl. Sci.* **2023**, *13*, 12567. [CrossRef]
9. Fekih, A. Fault-tolerant flight control design for effective and reliable aircraft systems. *J. Control. Decis.* **2014**, *1*, 299–316.
10. Zhang, Y.; Jiang, J. Bibliographical review on reconfigurable fault-tolerant control systems. *Annu. Rev. Control* **2008**, *32*, 229–252.
11. Liao, F.; Wang, J.L.; Yang, G.-H. Reliable robust flight tracking control: An LMI approach. *IEEE Trans. Control Syst. Technol.* **2002**, *10*, 76–89.
12. Xiang, Y.; Youmin, Z. Design of passive fault-tolerant flight controller against actuator failures. *Chin. J. Aeronaut.* **2015**, *28*, 180–190.
13. Ye, D.; Yang, G.-H. Adaptive fault-tolerant tracking control against actuator faults with application to flight control. *IEEE Trans. Control Syst. Technol.* **2006**, *14*, 1088–1096.
14. Yu, X.; Jiang, J. Hybrid fault-tolerant flight control system design against partial actuator failures. *IEEE Trans. Control Syst. Technol.* **2012**, *20*, 871–886.
15. Napolitano, M.R.; An, Y.; Seanor, B.A. A fault-tolerant flight control system for sensor and actuator failures using neural networks. *Aircr. Des.* **2000**, *3*, 103–128.
16. Sami, M.; Patton, R.J. Active fault-tolerant control for nonlinear systems with simultaneous actuator and sensor faults. *Int. J. Control Autom. Syst.* **2013**, *11*, 1149–1161.
17. Liu, M.; Cao, X.; Shi, P. Fuzzy-model-based fault-tolerant design for nonlinear stochastic systems against simultaneous sensor and actuator faults. *IEEE Trans. Fuzzy Syst.* **2013**, *21*, 789–799.
18. Alsaade, F.W.; Yao, Q.; Al-zahrani, M.S.; Alzahrani, A.S.; Jahanshahi, H. Neural-based fixed-time attitude tracking control for space vehicle subject to constrained outputs. *Adv. Space Res.* **2023**, *71*, 3588–3599.
19. Lin, C.; Wang, Z.; Yang, F. Observer-based networked control for continuous-time systems with random sensor delays. *Automatica* **2009**, *45*, 578–584.
20. Tong, S.; Huo, B.; Li, Y. Observer-based adaptive decentralized fuzzy fault-tolerant control of nonlinear large-scale systems with actuator failures. *IEEE Trans. Fuzzy Syst.* **2014**, *22*, 1–15.
21. Tong, S.; Li, Y.; Li, Y.; Liu, Y. Observer-based adaptive fuzzy backstepping control for a class of stochastic nonlinear strict-feedback systems. *IEEE Trans. Syst. Man Cybern. Part B (Cybern.)* **2011**, *41*, 1693–1704.
22. Xiao, B.; Yin, S.; Gao, H. Reconfigurable Tolerant Control of Uncertain Mechanical Systems with Actuator Faults: A Sliding Mode Observer-Based Approach. *IEEE Trans. Control. Syst. Technol.* **2017**, *26*, 1249–1258.
23. Li, B.; Hu, Q.; Yu, Y.; Ma, G. Fault-tolerant Attitude Control for Rigid Spacecraft. *IEEE Trans. Aerosp. Electron. Syst.* **2017**, *51*, 1216–1229.
24. Yu, X.; Fu, Y.; Zhang, Y. Aircraft fault accommodation with consideration of actuator control authority and gyro availability. *IEEE Trans. Control. Syst. Technol.* **2017**, *26*, 1285–1299.
25. Xie, D.; Lin, C.; Zhang, Y.; Sangwongwanich, A.; Ge, X.; Feng, X.; Wang, H. Diagnosis and resilient control for multiple sensor faults in cascaded H-bridge multilevel converters. *IEEE Trans. Power Electron.* **2023**, *38*, 11435–11450.
26. Xu, S.; Xu, X.; Wang, J.; Wang, H.; Chai, Y.; Chen, H.; Krishnamurthy, M. A Simultaneous Diagnosis Approach for Power Switch, Grid-Side Current Sensor, and DC-Link Voltage Sensor Faults in Single-Phase Three-Level Rectifiers. *IEEE Trans. Instrum. Meas.* **2024**, *73*, 2510416.
27. Xie, D.; Lin, C.; Lin, H.; Liu, W.; Du, Y.; Basler, T. OC Switch Fault Diagnosis, Pre-and Postfault DC Voltage Balancing Control for a CHBMC Using SVM Concept. *IEEE Trans. Power Electron.* **2024**, *39*, 677–692.
28. Wang, X.; Zhang, Y.; Wang, S. *Fault Tolerant Control of Large Civil Aircraft*; Springer Nature: Singapore, 2024.
29. Doostmohammadian, M.; Charalambous, T. Distributed Anomaly Detection and Estimation over Sensor Networks: Observational-Equivalence and $ Q $-Redundant Observer Design. In Proceedings of the 2022 European Control Conference (ECC), London, UK, 12–15 July 2022; IEEE: Piscataway, NJ, USA, 2022; pp. 460–465.

30. Cao, Y.; Ren, W. Optimal linear-consensus algorithms: An LQR perspective. *IEEE Trans. Syst. Man Cybern. Part B (Cybern.)* **2009**, *40*, 819–830.
31. Friedland, B. *Control System Design: An Introduction to State-Space Methods*; Courier Corporation: North Chelmsford, MA, USA, 2012.
32. Ferrante, A.; Ntogramatzidis, L. The generalised discrete algebraic Riccati equation in linear-quadratic optimal control. *Automatica* **2013**, *49*, 471–478.
33. Wang, X.; Liao, R.; Shi, C.; Wang, S. Linear extended state observer-based motion synchronization control for hybrid actuation system of more electric aircraft. *Sensors* **2017**, *17*, 2444. [CrossRef]
34. Hanke, C.R.; Nordwall, D.R. *The Simulation of a Jumbo Jet Transport Aircraft. Volume 2: Modeling Data*; NASA: Washington, DC, USA, No. NASA-CR-114494; 1970.
35. Apkarian, P. Continuous-time analysis and H_2 multi-channel synthesis with enhanced LMI characterizations. *IEEE Trans. Automat. Contr.* **2001**, *46*, 1941–1946.
36. Zhang, F. *The Schur Complement and Its Applications*; Springer Science & Business Media: Berlin, Germany, 2006; Volume 4.

Disclaimer/Publisher's Note: The statements, opinions and data contained in all publications are solely those of the individual author(s) and contributor(s) and not of MDPI and/or the editor(s). MDPI and/or the editor(s) disclaim responsibility for any injury to people or property resulting from any ideas, methods, instructions or products referred to in the content.